Journal of Environmental Chemical Engineering 10 (2022) 108708

Contents lists available at ScienceDirect

Journal of Environmental Chemical Engineering

journal homepage: www.elsevier.com/locate/jece

Advanced method for clean water recovery from batik wastewater via sequential adsorption, ozonation and photocatalytic membrane PVDF-TiO_2/rGO processes

Tutuk Djoko Kusworo [a,*], Irvan [b], Andri Cahyo Kumoro [a], Yasmin Nabilah [a], Aufa Rasendriya [a], Dani Puji Utomo [a], Hasrinah Hasbullah [c]

[a] Department of Chemical Engineering, Faculty of Engineering, Universitas Diponegoro, Semarang 50275, Indonesia
[b] Department of Chemical Engineering, Universitas Sumatera Utara,Jalan Almamater Komplek USU, Medan 20155, Indonesia
[c] School of Chemical and Energy Engineering, Faculty of Engineering, Universiti Teknologi Malaysia, Skudai 81310, Johor, Malaysia

ARTICLE INFO

Keywords:
Adsorption
Band gap energy
Hydrophilicity
Fouling
Ozonation
Photocatalytic membranes

ABSTRACT

This study aimed to investigate the synthesis of TiO_2/rGO nanocomposite particles and incorporate them into PVDF membrane for Batik wastewater treatment. Bentonite adsorption and ozonation were combined to mitigate fouling development during the filtration process. The results proved that the TiO_2/rGO nanocomposite successfully narrowed the band gap energy ~2.9 eV by which enhancing its photo sensitivity within the visible light region. Furthermore, the chemical compatibility of TiO_2 with PVDF can be improved with the presence of rGO. PVA coating on PVDF-TiO_2/rGO membrane has enhanced hydrophilicity and provided the best performance by giving permeate flux ~19.3 $L.m^{-2}.h^{-1}$ and dyes rejection up to ~90%, respectively. Obviously, pre-treatment using bentonite and followed by ozonation significantly enhanced the permeate flux up to 21 $L.m^{-2}.h^{-1}$ and overall rejection up to ~95%. As expected, the addition of TiO_2/rGO nanocomposites increased membrane's photocatalytic activity by 30–100%. More importantly, wastewater treatment by combining bentonite adsorption, ozonation, and photocatalytic membrane filtration has successfully improved permeate flux and performance stability, reduced fouling growth, and produced clean water. Therefore, the results of this study offers a new promising advanced wastewater treatment for Batik wastewater treatment to produce clean water.

1. Introduction

Since UNESCO designated Batik as a world heritage in 2009, Batik textile industries have enjoyed steady growth due to the increasing demand for its unique fashion trend [1]. Unfortunately, Batik industry can be regarded as one of the industrial sectors that produce large amount of highly contaminated and toxic wastewater. Textile industry is reported to continuously contribute 17–20% of the global water pollution [2]. Commonly, Batik wastewater is generated from the coloring, soaking, washing and wax removal processes [3]. Obviously, Batik wastewater contains typically pollutant substances, such as dyes, starch, aluminum sulfate, and wax with extreme pH, high COD, BOD, TSS and intense color that exceeds the quality standards for wastewater disposal [4]. Moreover, the use of synthetic reactive dyes may terrifically deteriorate water quality due to its high toxicity and non-biodegradability [5]. Therefore, an appropriate wastewater management is crucial before its discard to the environment.

To date, numerous physicochemical methods have been developed for Batik wastewater treatments, such as chemical coagulation-precipitation, adsorption, electrocoagulation, flocculation, and advanced oxidation. In addition to being cost intensive, these methods generally produce a large amount of complex sludge and low water product quality. Membrane separation offers excellent performance in wastewater treatment and water reclamation. There have been several membrane contactors for Batik wastewater treatment, such as direct filtration using pressure-driven membranes (UF, NF, RO), membrane distillation (MD), membrane bioreactor (MBR), and membrane electrodialysis (ED). Rashidi et al. [6] developed UF/NF membrane filtration system for Batik wastewater treatment and successfully removed up to 95% resin and wax. Laqbaqbi et al. [7] utilized direct contact membrane distillation (DCMD) for textile wastewater treatment, which provided ~99% dye removal. However, DCMD method consumed high energy

* Corresponding author.
E-mail address: tdkusworo@che.undip.ac.id (T.D. Kusworo).

https://doi.org/10.1016/j.jece.2022.108708
Received 8 June 2022; Received in revised form 24 August 2022; Accepted 2 October 2022
Available online 6 October 2022

supply to allow phase change. Lafi et al. [8] utilized hybrid process of UF/electrodialysis for textile wastewater treatment, which was able to remove soluble contaminants up to 97%. MBR is a hybrid process of biological treatment and membrane filtration that has been extensively developed for wastewater treatment. Febriasari et al. [9] reported 86% dyes removal in Batik wastewater treatment using membrane bioreactor. Although membrane-based processes have become more attractive in wastewater treatments, their current applications remain susceptible to fouling growth that leads to performance decline and operating cost increase. The development of anti-fouling or reduced-fouling membrane materials by either bulk or surface modification can be an alternative solution to overcome the fouling problem.

Many research groups have developed antifouling membrane through hydrophilic nanoparticle loading [10], surface grafting [11], in-situ polymerization [12], layer-by-layer assembly [13], and photocatalyst incorporation [14]. Among those proposed methods, the combination between photocatalysis and membrane filtration system has been reported to significantly reduce fouling, extend membrane lifetime, and improve pollutant removal performance by allowing simultaneous photocatalytic degradation of the pollutants [15]. As for the semiconductor photocatalysts, titanium dioxide (TiO_2) exhibited the highest photoactivity potential due to its strong photocatalytic activity, abundant availability, and low cost. As expected, the inclusion of low amount of TiO_2 into PVDF membrane has been found to cause ~99% removal of methylene blue [16]. However, the wide band gap energy of TiO_2 (~3.2 eV) has restricted its application for photocatalysis where the photodegradation is merely triggered by UV-light. In this regard, numerous efforts have been devoted to reduce the band gap energy bellow 3.2 eV and to shift the photon absorption of TiO_2 to visible light. Elemental doping such as N, P, C, S into TiO_2 photocatalyst have significantly reduced the band gap energy through electronic band structure modification and simultaneously improved its response in the visible light [17]. Haq et al. [18] also reported that annealing of TiO_2 particles could decrease the band gap energy by enhancing their crystallinity and packing density. The binary composite material of TiO_2 and two-dimensional carbonaceous material, such as graphene, graphene oxide (GO), and reduced graphene oxide (rGO) can be a promising candidate because they facilitate the transfer of photogenerated electrons and holes as well as reducing particle aggregation tendency [19]. rGO is two dimensional carbon material derived from GO through reduction process with zero band gap energy, large specific area, and unique electrical properties that provide suppression of e^-/h^+ pair recombination [20]. Yu et al. [21] developed ^2D–^2D rGO-TiO_2 nanocomposite through solvothermal with the narrowed band gap energy of 2.77 eV and more importantly, the nanocomposite material has provided impressive dye removal and self-cleaning ability under visible light. Table 1 summarizes previous reported studies regarding the photovcatalytic membrane application for various industrial pollutants and dyes. Herein, the TiO_2/rGO nanocomposite was synthesized and incorporated into PVDF membrane to be employed as a photocatalytic membrane for Batik wastewater treatment.

Based on the previous reports that the photocatalytic membranes (PMs) provided significant fouling reduction, its direct application to treat the highly contaminated Batik wastewater will be unveiled. To provide a more comprehensive perspective, the combined processes, namely adsorption and ozonation as pre-treatments will also be adopted to mitigate the fouling problem. Ozone is an environmentally friendly oxidizing agent that is widely used in drinking water and wastewater treatment. In an aqueous system, ozone oxidizes organic compounds by direct oxidation with O_3 molecules or formation of hydroxyl free radicals [22]. Several researchers also reported that ozone pretreatment is an effective way to degrade natural organic colloids (or biogenic

Table 1
Summary of previous reported works on the photocatalytic membrane applications for pollutants and dyes removal.

Membrane material	Catalyst	Preparation method	Pollutant	Results	Ref.
Polyvinylidene fluoride (PVDF)	$ZnO/Ag_2CO_3/Ag_2O$	Blending	Ibuprofen	The ibuprofen removal from 27.37% in dark conditions to 35.27% under UV light irradiation using the PVDF- $ZnO/Ag_2CO_3/Ag_2O$ composite membrane.	[25]
Polyacrylonitrile (PAN)	Ag@ZnO	Hydrothermal	Methyl orange (MO)	The decorated membrane possessed both photocatalytic and antibacterial properties. After 5 cycles of photodegradation, the photocatalytic activity remained at 98.6%.	[26]
TiO_2/Al_2O_3 ceramic membrane	TiO_2/Al_2O_3	Sol-gel	Direct Black 168	Dye removal of 82%. The membranes' photocatalytic properties helped in permeate flux improvement and prevented fouling formation.	[27]
Cellulose	ZnO nanosheets	Blending	Methyl orange (MO), phenol, and aniline	The ZnO/CFR12 composite membrane with the highest ZnO flower/sheet ratio exhibited the best photocatalytic performance (the degradation rate of MO, phenol, and aniline were 95.44%, 100%, and 82.39%, respectively).	[28]
Polypiperazine amide (PPA)	ZnO-PEG	Blending	Industrial dye wastewater	ZnO-PEG/UF PPA membrane presented SDWW degradation (100%), turbidity removal (100%), COD reduction (97.37 ± 0.06%), and electrical conductivity removal (92.38 ± 0.66%). The modified membrane also showed an outstanding antifouling property.	[29]
Polyethylene oxide (PEO)	$CNT/ZnO/TiO_2$	Hydrothermal	Acid orange 7 (AO7)	The $CNT/ZnO/TiO_2$ nanocomposite membrane integrated the advantages of multiple semiconductors and carbon-based materials to exhibit high mechanical strength along with high photocatalytic capability, which possessed the ability to produce clean water at a high membrane flux with low fouling potential.	[30]
Polysulfone (PSf)	TiO_2-GO	Blending	Methylene blue (MB)	The composite membrane exhibited 3–4 times faster dye removal under UV and sunlight. Composite addition increased the membranes' hydrophilicity.	[31]
Polyvinylidene fluoride (PVDF)	$CdS/Bi_2WO_6/ZnO$	Blending	Nitrile	The photocatalytic activity of the hybrid membrane was evaluated, and 92.58% of the nitrile was converted into non-toxic substances within 4 h under simulated sunlight irradiation	[32]
Polyvinylidene fluoride (PVDF) + Polypropylene (PP)	TiO_2	Blending	4-nitrophenol (4-NP)	50% removal efficiency of 4-NP after 5 h of irradiation. The 4-NP concentration in permeate was equal in retentate.	[33]
Polyvinylidene fluoride (PVDF)	TiO_2/rGO and PVA coating	Blending and coating	Industrial dye wastewater	The membrane porosity, hydrophilicity, and water absorption ability are all improved with the addition of the TiO_2/rGO photocatalyst. In addition, the PVA coated PVDF-TiO_2/rGO membrane showed outstanding performance in terms of permeate flow, pollutant rejection, photo-degradation stability, and antifouling properties	This work

colloids), which potentially promote membrane fouling [23], [24]. In this study, the ozonation was combined with adsorption using bentonite to reduce organic contaminants of the raw Batik wastewater prior to photocatalytic membrane filtration process. Natural bentonite clay was selected as the adsorbent due to its high surface area, excellent adsorption capacity, and low-cost. Nanocomposite photocatalyst synthesis, photocatalytic membrane fabrication, characterization and performance evaluation in Batik wastewater treatment were evaluated in a laboratory-scale membrane filtration cell. The combination of the bentonite adsorption, ozonation pre-treatment processes and photocatalytic PVDF-TiO_2/rGO membrane filtration is expected to be an efficient process for recovering clean water from Batik wastewater.

2. Materials and methods

2.1. Materials

The polyvinylidene fluoride (PVDF) Solef® 6020/1001 was purchased from Solvay Advanced Material, USA, while the N-Methyl Pyrrolidone (NMP) as a solvent was purchased from Merck, Singapore. Graphite powder (<20 nm) and glutaraldehyde 50 wt% in H_2O were the product of Sigma Aldrich, Singapore, while TiO_2 nanoparticles was purchased from Shanghai Chemicals Ltd, China. The first grade polyvinyl alcohol (PVA) with 1000 polymerization degree and completely hydrolyzed was supplied by Wako Pure Chemical, Japan. Other chemicals, such as H_2SO_4, $KMnO_4$, H_3PO_4, HCl, and $NaNO_3$ were procured from Merck, Singapore. Bentonite clay granule was supplied by Brataco Chemika, Indonesia. The reduced graphene oxide (rGO) was prepared from graphite powder according to the modified Hummer's method as presented in previous study [34]. The raw Batik wastewater sample was collected from the Kampoeng Batik, Batik's textile industry, Semarang, Indonesia with the initial characteristics as tabulated in Table 2.

2.2. PVDF/TiO_2-rGO photocatalytic membrane fabrication

The PVDF/TiO_2-rGO photocatalytic membrane was prepared using the bulk-blending method and followed by the dry-wet phase inversion technique according to the protocol used in the previous work [35]. TiO_2-rGO nanocomposite as photocatalyst filler was synthesized according to the method previously used by Leal et al. [36] with the rigorous procedure was available in the supplementary material **Text S1**. Polymeric solution and nanoparticle suspension were prepared separately to prevent nanoparticles agglomeration. Polymeric solution was prepared by dissolving a predetermined amount of PVDF polymer in NMP solvent to an exact 16 wt% and stirred at 60–70 °C until the achievement of a homogenous solution. The TiO_2-rGO nanocomposite particles were dispersed into NMP solvent in another container and the mixture was further ultrasonicated for 30 min to obtain a stable and homogenous suspension. Then, this nanoparticles suspension was introduced to the polymeric solution and was followed by vigorous stirring for 6–8 h at 60–70 °C until the formation of a homogeneous solution. Prior to casting onto a clean glass plate using a casting knife with 150 μm thickness, the dope solution was left under vacuum for 2 h to allow the removal of trapped bubbles. The polymer film on the glass plate was allowed within 30 s for solvent evaporation then subsequently immersed into a coagulation bath containing deionized water at 30 °C for 24 h to obtain a flat sheet membrane. The fabricated membrane was dried at room temperature overnight. The neat PVDF, PVDF/TiO_2, and PVDF/rGO were also fabricated and further used as the control for membrane performance comparison. The PVDF/TiO_2-rGO membrane surface was then modified for improving surface hydrophilicity and morphological properties via crosslinked PVA coating following the procedure previously used by Kusworo et al. [37] (the detail of the modification procedure was available in the supplementary material **Text S2)**.

Table 2
Characteristics of Batik Wastewater from Kampoeng Batik Semarang, Indonesia.

Parameters	Value	Standard*
Chemical oxygen demand (COD), mg.L^{-1}	668.24	250
Biochemical oxygen demand (BOD), mg.L^{-1}	386.63	85
Total Suspended Solid (TSS), mg.L^{-1}	1280	60
Total dissolved solids (TDS), mg.L^{-1}	4454	500
Oil and grease, mg.L^{-1}	6.78	5.0
pH	5.9	6.0 – 9.0
Cr Hexavalent, mg.L^{-1}	2.17	2.0
Color absorbance, a.u.	0.772	colorless

* Quality standard of industrial wastewater according to the Ministry of Environment and Forestry the Republic of Indonesia.

2.3. Characterization

The surface and cross-sectional morphology of the fabricated membranes were assayed using scanning electron microscope (SEM, JEOL Series LA, Japan) and transmission electron microscope (TEM, JEOL JEM-1400 Series, Japan). Then, their elemental compositions were identified using the energy dispersive x-ray (EDX, JEOL Series LA, Japan) and x-ray diffraction (XRD, PANalytical XRD X′pert3 powder DY 5367, UK). The Fourier transform infra-red spectrophotometry (FTIR, Perkin Elmer PC1600, USA) was performed to characterize the chemical functional groups present in the PVDF-rGO-TiO_2 membranes at wavenumber range of 4000–450 cm^{-1}. The photocatalytic properties of the nanocomposite fillers were assessed using the optical analysis of diffuse reflectance spectrometry (DRS) method by a UV-Vis spectrophotometer (Shimadzu, Japan) at wavelength range of 250 – 700 nm. In addition, the surface charges of the photocatalyst nanocomposite were determined using point of zero charge method (PZC) according to the previous studies [38], [39], where the rigorous procedure was provided in supplementary material S3. The surface hydrophilicity and wettability of the membranes were evaluated based on the contact angle measurement (Dataphysics-instrument OCA 25, Germany) at room temperature. From the contact angle measurement, the surface energy of the membrane was further calculated using Fowkes theory as expressed in Eqs. (1) and (2).

$$\frac{(1+\cos\theta)\gamma_L}{2} = \sqrt{\gamma_L^D\gamma_S^D} + \sqrt{\gamma_L^P\gamma_S^P} \tag{1}$$

$$\gamma_S = \gamma_S^D + \gamma_S^P \tag{2}$$

where θ is the apparent contact angle (deg). γ_L^D, γ_L^P, γ_S^D, and γ_S^P are the dispersive and polar interfacial surface energy of the liquid and solid state, respectively.

Membrane porosity (ε) and pore size (r_m) were indirectly estimated using the gravimetric and pure water permeability methods, respectively. The ε value was calculated using Eq. (3), whereas the r_m value was calculated using the Guerout-Elford-Ferry equation for pore flow model Eq. (4).

$$\varepsilon = \frac{w_2 - w_1}{A \times l \times \rho} \tag{3}$$

$$r_m = \sqrt{\frac{(2.9 - 1.75\varepsilon)8\eta l Q}{\varepsilon \times A \times \Delta P}} \tag{4}$$

where w_1 and w_2 are the mass of the dried and wet membranes, respectively (kg). Accordingly, A is the membrane surface area (m^2), l is the membrane thickness (m), Q is volume of pure water permeate per unit time (m^3.s^{-1}), ρ is the pure water density at 25 °C (997 kg.m^{-3}), η is the pure water viscosity at 25 °C (8.9 ×10^{-4} Pa.s), and ΔP is the transmembrane pressure (Pa).

2.4. Experimental setup and procedures

In this work, the Batik wastewater treatment process was conducted in two stages: (1) pre-treatment using bentonite adsorption-ozonation process and (2) photocatalytic membrane filtration as clearly illustrated in Fig. 1. The commercial bentonite clay powder was washed, activated using acid treatment method and dried at 105 °C for 24 h according to the previous studies [40], [41]. A batch process was carried out to allow wastewater adsorption under continuous agitation using various amount of bentonite (0.5, 1.0, 1.5, and 2.0) g of bentonite for every 100 mL Batik wastewater. The adsorption process was conducted for (30, 60, ad 90) min for each batch until the achievement of equilibrium. The adsorbent was then separated from the wastewater via gravity settling. Accordingly, the adsorption treated wastewater was further ozonated in semi-batch mode with constant ozone injection rate of 3000 mg O_3/h for 180 min. In order to facilitate maximum ozone transfer efficiency into wastewater, a baffled tank reactor equipped with two ozone diffusers at its bottom was used. The effluent of the ozonation reactor was then continuously delivered to the membrane cell equipped with UV lamp type C (Phillips TUV 30-watt, Netherland) for photocatalytic membrane filtration process. The permeate water was withdrawn for further analysis and the retentate was recycled to the ozonation reactor tank.

2.5. Permeate water flux

A crossflow filtration system evaluated the membrane permeation flux. Firstly, the tested photocatalytic membrane was compacted using deionized (DI) water for 30 min at constant trans-membrane pressure of 5 bar. Then, the crossflow filtration experiment was performed at an operating pressure of 5 bar. For each tested membrane, the permeate water was collected every 30 min during filtration process. The permeate flux was subsequently calculated using Eq. (5).

$$J = \frac{V}{A \times t} \tag{5}$$

where J is the permeate flux (L.m^{-2}h^{-1}); V is the permeate volume (L); A is the effective membrane area (m^2), and t is the permeation time (h).

2.6. Pollutants rejection evaluation

The pollutants removal from Batik wastewater was evaluated based on the COD, TDS, and color concentration in both feed and permeate. Then, those parameters were calculated to determine the pollutants rejection rates according to Eq. (6).

$$R = \left(1 - \frac{C_p}{C_f}\right) \times 100\% \tag{6}$$

where R is rejection efficiency (%); C_p and C_f are the concentration of the pollutants in permeate and feed solution, respectively (mg.L^{-1}).

2.7. Photocatalytic degradation and kinetic evaluations

The photocatalytic activity of the fabricated membranes were examined by analyzing the organic degradation rate, which can be easily identified by the COD decline. The raw Batik wastewater was used as the feed. Then, the membrane was hermetically attached to a glass slide and the glass was further immersed into Batik wastewater in an observation vessel. The vessel was positioned in the dark environment for 60 min before subjecting the sample under a UV lamp to initiate adsorption equilibrium to ensure that only photocatalytic activity was examined in the experiment. The experiment was performed for 120 min, from which an equal aliquot was sampled every 30 min from the vessel to measure its COD level. Furthermore, a photocatalytic activity modeling was proposed to provide a clear approach to the photodegradation of organic matters. The kinetic behavior of photodegradation of the fabricated membranes were modelized using three models including the zero order kinetic, Langmuir-Hinshelwood, and second order kinetic, as the mathematical expressions are represented in Eqs. (7)–(9), respectively.

$$C_o - C = k_o t \tag{7}$$

$$\ln\left(\frac{C_o}{C}\right) = k_1 t \tag{8}$$

$$\frac{1}{C} - \frac{1}{C_o} = k_2 t \tag{9}$$

Where C_o and C represent the initial and certain concentrations of COD (mg/L), t represents time (min), k_o (mg/L min), k_1 (min^{-1}), and k_2 (L/

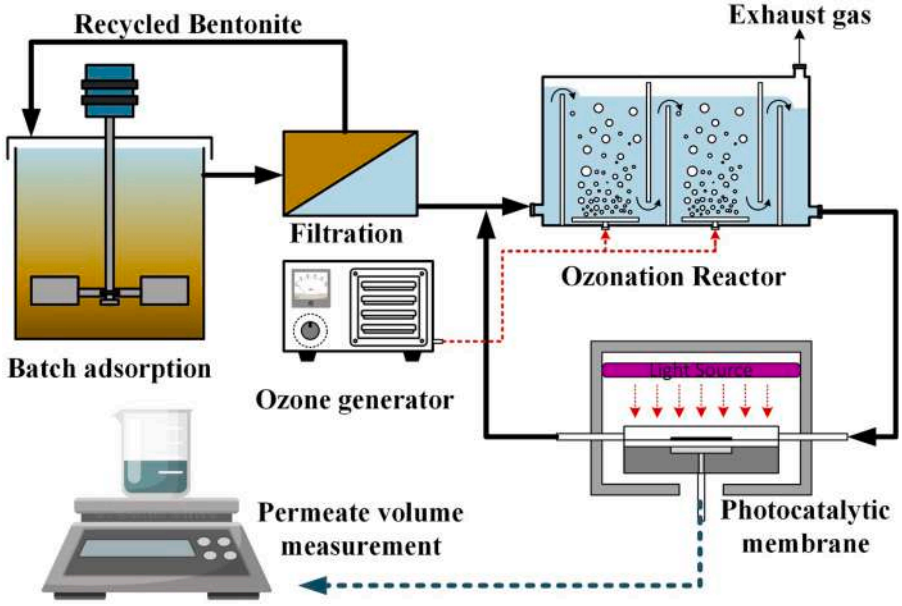

Fig. 1. Simplified illustration of advanced membrane filtration with bentonite adsorption and ozonation as pre-treatment for Batik wastewater treatment.

mg min) show the rate constants for zero order, Langmuir-Hinshelwood, and second order kinetic models, respectively.

2.8. Membrane fouling and stability test

The influence of pre-treatment and photocatalytic degradation on the mitigation of membrane fouling was evaluated quantitatively using the resistance-in-series model [42].

$$R_m = \frac{TMP}{\eta J_0} \tag{10}$$

$$R_f = \frac{TMP}{\eta J_1} - R_m \tag{11}$$

$$R_c = \frac{TMP}{\eta J_2} - R_m - R_f \tag{12}$$

where R_m, R_f, and R_c are the intrinsic membrane resistance, resistance of adsorbed solute on the membrane pores of walls, and resistance formed by reversible cake layer, respectively (m^{-1}). *TMP* is the trans-membrane pressure (Pa). η is the dynamic viscosity of DI water at room temperature (Pa.s). J_0, J_1, and J_2 are the pure water permeate flux of clean membrane, hydraulic cleaned membrane, and fouled membrane, respectively ($m.s^{-1}$). In addition, to further explore of the photocatalytic membrane stability after sequential hydraulic cleaning, a cycle test [43] of Batik wastewater filtration under UV-light irradiation was also carried out.

3. Results and discussions

3.1. Characteristics of TiO_2/rGO nanocomposite

To obtain an in-depth understanding of the photodegradation behavior during wastewater treatment application, the synthesized nanocomposite photocatalyst was characterized for its physicochemical properties. Based on their SEM and TEM images, Fig. 2(a) confirms that the TiO_2 particles were in nanometer size with irregular structure. Furthermore, the particle size distribution analysis showed that their average particle size was ~100 nm. Fig. 2(b) shows the SEM image of rGO with single layer structure indicating the successful exfoliation. The detailed structure of TiO_2 and TiO_2/rGO nanocomposite were identified using TEM images as presented in Fig. 3. The size of TiO_2 was estimated to be in the range of 50 – 200 nm. The TEM image revealed a layered structure of rGO that has creases due to hydrothermal reduction. TiO_2 clusters are clearly attached and inhomogeneously dispersed over rGO nanosheet. The thickness of rGO nanosheet was estimated to be less than 1 nm from the edges and wrinkles. The rGO nanosheets provide two-dimensional "mattress"-like structure with TiO_2 nanoparticle attached over the sheets.

Material phase, crystal structure, and crystalline nature of the materials used in this study were analyzed using powder x-ray diffraction. Fig. 4(a) presents XRD patterns of graphite, GO, rGO, and TiO_2/rGO nanocomposite. Graphite demonstrates one prominent peak at 2θ of 26.42° which corresponds the presence of well-arranged layer structure with 0.3370 nm D-spacing. For GO XRD pattern, the peak was shifted to 11.14° with D-spacing of 0.7933 nm. The increasing of D-spacing was attributed to the intercalation of oxide functional groups indicating that the graphite was fully oxidized into GO. The GO reduction process using Na_2CO_3 as reducing-agent partially eliminated the oxygen-containing functional groups indicated by appearance of boarder peak for rGO at 2θ of 24.88° and the presence of peak at 2θ of 11.84° belongs to the unreduced oxygen-containing groups. The D-spacing of rGO was 0.3572 nm lower than that of GO D-spacing, it indicates the restoration of π-conjugated structure of rGO. For TiO_2/rGO nanocomposite, the XRD pattern showed sharp peak at 2θ of 25.69° (101), 37.27° (013), 38.15° (004), 38.83° (112), 48.39° (200), 54.25° (015) that exactly correspond with the TiO_2 anatase pattern based on "Match! 3″ software analysis.

The FTIR spectra of rGO in Fig. 4(b) showed characteristic peaks at 1736 cm^{-1} and 1218 cm^{-1} that belong to the carbonyl and carboxyl stretching. It could be due to the residual oxygen containing groups of unreduced part of rGO. This result supported XRD data where the GO was partially reduced. The FTIR spectra further confirms the existence of TiO_2 based on the appearance of an IR absorption peak at fingerprint region of 474 – 480 cm^{-1} of the FTIR spectra. A similar observation was reported by Ayodhya et al. [44] regarding the presence of metal oxide bond of TiO_2 based on the appearance of an IR absorption of Ti-O bending at about 680 cm^{-1}. This absorption band difference could be due to the distinct TiO_2 structural phase. Typically, TiO_2 exists in three types polymorph: anatase, rutile, and brookite with anatase and rutile are the two main structural phases of TiO_2 [45]. The broad band at 3427 cm^{-1} and 1564 cm^{-1} belong to the stretching and bending vibration of -OH and Ti-OH, respectively. These observations represent the adsorbed water as the result of the interaction between the hydrophilic TiO_2 nanoparticles with water molecules. Additionally, the broad peak observed peaks at 3437 cm^{-1} which may related to the absorbed -OH due to the interaction of O-Ti-O and H-O-H molecule. The peaks at 1564 cm^{-1} and 474 cm^{-1} that correspond to Ti-OH and Ti-O stretching absorption. The appearance of small peaks of TiO_2/rGO FTIR spectra could be attributed to the unreduced oxygen-containing functional group of rGO. Hence, the observed absorption peaks that correspond to the specific vibration of TiO_2 and rGO indicated a successful synthesis of TiO_2/rGO nanocomposite. A previous report suggested that the water-adsorbing behavior of TiO_2/rGO nanocomposite plays important role in photocatalytic activity [46].

Light absorption behavior of the manufactured TiO_2/rGO

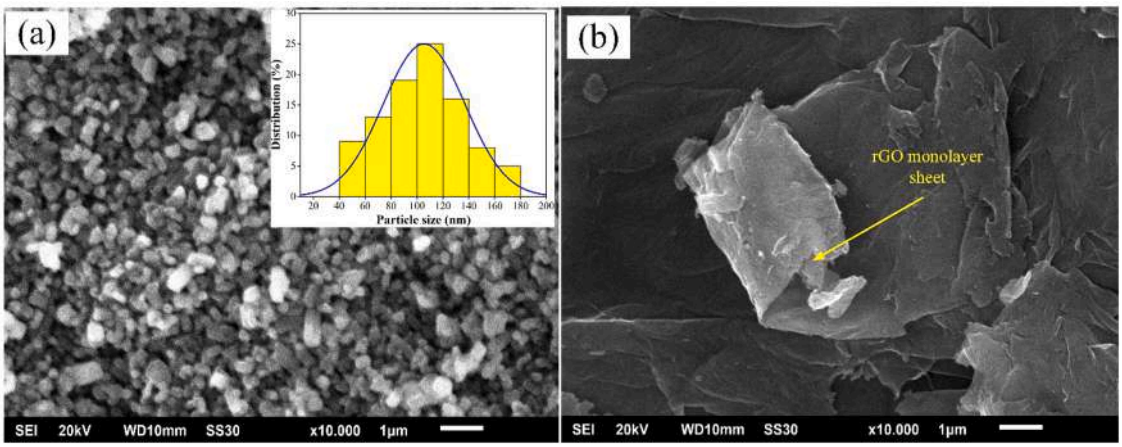

Fig. 2. SEM images of (a) pure TiO_2 nanoparticles and (b) rGO nanosheets.

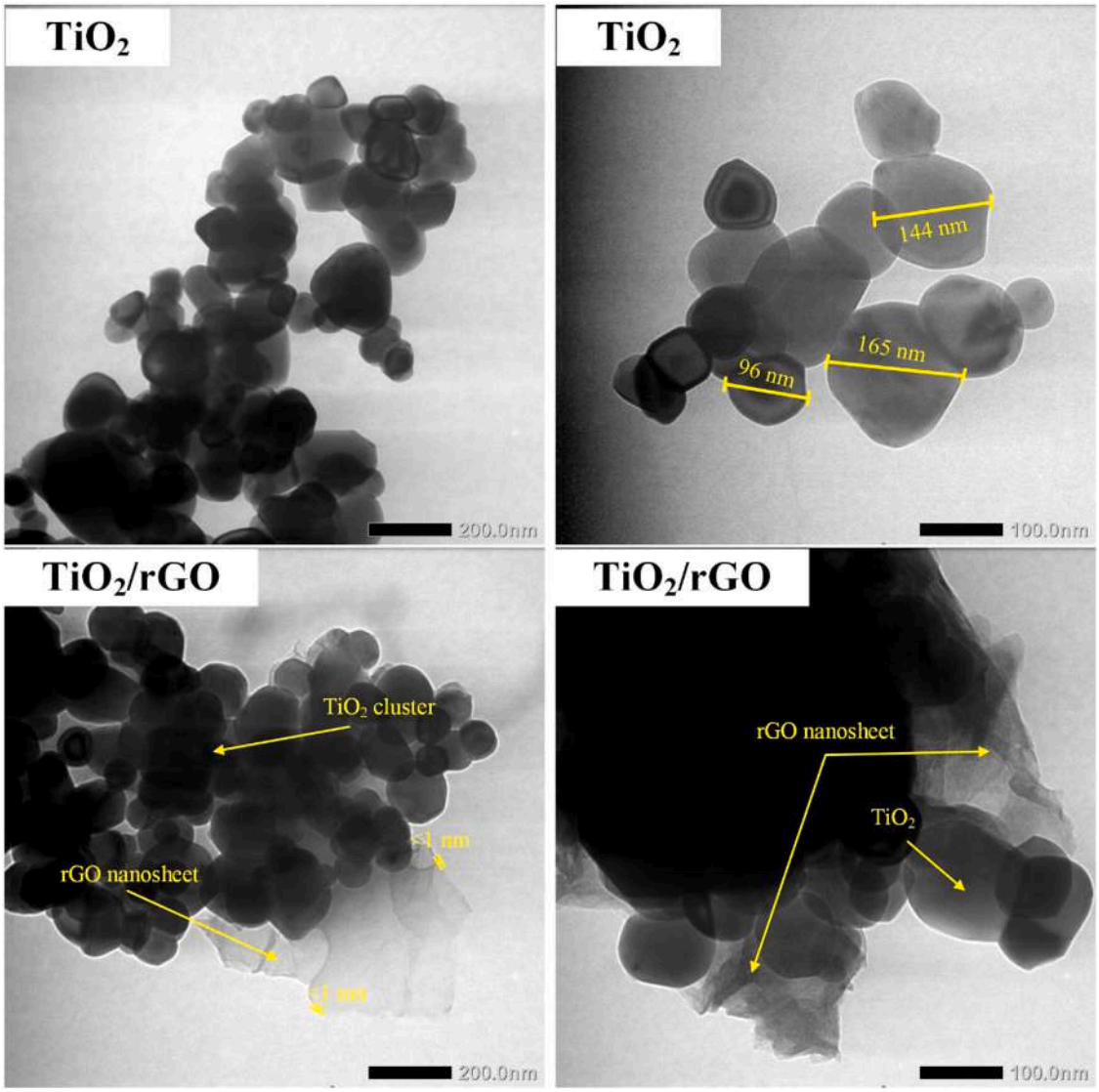

Fig. 3. TEM images of pure TiO_2 and TiO_2/rGO nanocomposite materials.

nanocomposite was evaluated using UV-Vis DRS measurement that disclose the optical properties of a photocatalyst. The UV-Vis DRS plots of TiO_2/rGO nanocomposite photocatalyst, pure TiO_2 and rGO are presented in Fig. 5(a). All tested materials exhibited their specific light response behaviors. As expected, TiO_2 has strong absorption at UV region and decrease sharply at visible light region. This observed characteristic could be due to the high band gap energy of TiO_2 (~3.2 eV) thereby it requires high *hv* energy to facilitate electron transition from valence band (CB) to conduction band (VB). Meanwhile, rGO was found to be a non-photoactive material as indicated by a low overall photon absorption. Nevertheless, the light absorption of rGO at the visible region is higher than that of TiO_2. The UV-Vis DRS of the TiO_2/rGO nanocomposite exhibited obvious red shift at the visible region compared with pure TiO_2. The high electron mobility of rGO played important role in improving the charge transfer properties of the nanocomposite material leading to a higher photo sensitivity [47]. Fig. 6 (b) exhibits the Tauc's plot of photon energy (*hv*) level versus the quantity of absorbed energy $(\alpha hv)^{\gamma}$ for the determination of the band gap energy of the fabricated materials. It is clearly observed that the pure TiO_2 showed band gap energy of 3.20 eV that is a typical band gap of anatase phase. However, the band gap energy of rGO could not be determined using Tauc's plot because the slope is too low. A previous report mentioned that rGO is a two-dimensional carbon material with zero band gap energy [48]. The observed band gap energy of the TiO_2/rGO nanocomposite was 2.90 eV, which is lower than that of TiO_2. This narrowing band gap of the nanocomposite photocatalyst could be associated to the improved planar structure which induces reflection [49]. In addition, Gonçalves et al. [50] also explained that the decrease of band gap is associated with both interaction of TiO_2 and rGO and the formation of Ti-O-C bonds. The results suggested that the combination of TiO_2 and rGO with a band gap energy and an increased visible light absorption would contribute to increase the photocatalytic activity.

Fig. 6(a) depicts the specific surface area of the mesoporous structure of TiO_2 and TiO_2/rGO nanocomposite obtained from the nitrogen adsorption-desorption profile of the BET-BJH analysis. The tested materials (TiO_2 and TiO_2/rGO) showed adsorption-desorption type IV(a) isotherm indicated the typical adsorption behavior of mesopores consists of multilayer adsorption. The hysteresis loops were type H2(b) which resembles of complex pore structure resulting in adsorption metastability and delayed desorption branch [51]. The estimated surface areas of the nanocomposites photocatalyst and TiO_2 were 232 and 186 m^2/g, respectively. These results suggest that the combination of TiO_2 and rGO has successfully increased the specific surface area. This improvement can be associated with the two-dimensional structure of reduced graphene oxide. rGO materials is graphene like material with large surface area. Basically, the theoretical specific surface area of

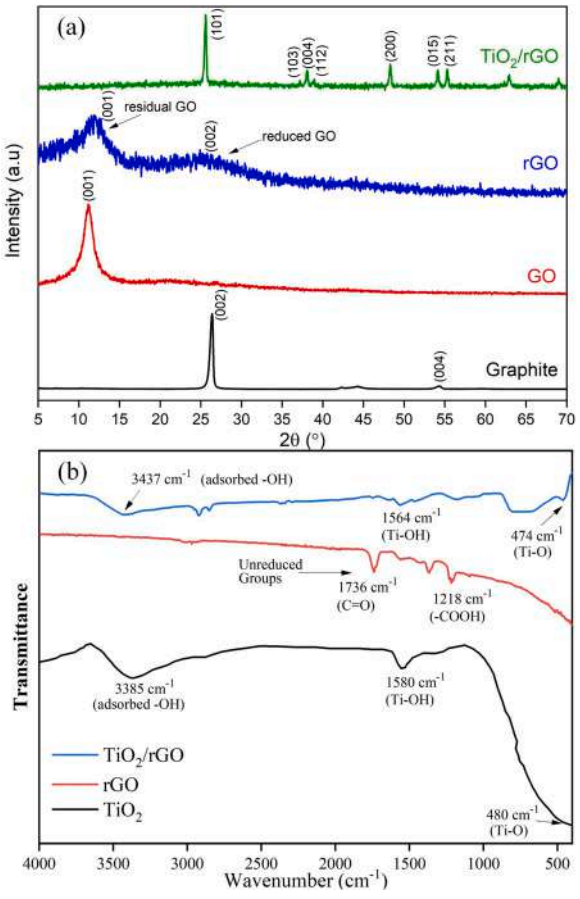

Fig. 4. (a) XRD pattern and (b) FTIR spectra of modified membrane fillers.

graphene is 2640 m^2/g [52]. A higher surface area of nanocomposite is advantageous for photocatalytic reaction due to the provision of massive active sites. Fig. 6(b) presents the pH changes of the aqueous solutions from their initial pH at 25°C for 48 h as the result of OH^- or H^+ ions desorption on the tested material surface. Point of zero charge (PZC) of the materials defines the condition of the solution in which the surface density of positive charges equals that of negative charges [53]. The pH_{PZC} value describes the surface charge potential of the material as an alternative for zeta potential analysis. The pH_{PZC} of TiO_2, rGO, and TiO_2/rGO were 5.98, 3.30, and 4.85, respectively. The significance of this analysis is that the tested material possesses positive charge at the solution with pH values less than the PZC and vice versa. The results of PZC analysis is important properties for understanding the mechanism of Donnan's exclusion of charged membrane surface.

3.2. Characteristics of PVDF-TiO_2/rGO photocatalytic membrane

3.2.1. Photocatalytic membrane morphology

Fig. 7 depicts the surface and cross-section morphology of the fabricated membranes. The evaluation of morphological properties plays a pivotal role in appraising the microstructural changes of the membranes caused by any kind of modification attempts. As clearly seen in Fig. 7, all tested membranes possess a relatively smooth surface. However, the neat PVDF membrane also exhibited some surface defects. This phenomenon could happen due to three possible causes, such as diverse coagulation rates of the whole membrane during phase inversion, uncontrolled air humidity during membrane drying process, and failure of mechanical casting. Such defects on the membrane surface could potentially develop unselective void formation and thus reduce the membrane selectivity performance. Moreover, they also could initiate polymer crack under pressurized condition that shorten membrane's durability and lifetime. As expected, membrane with TiO_2/rGO loading showed better surface morphology than that of neat PVDF membrane with fewer and smaller defect spots. The evenly distributed white nodules over the membrane surface can be associated with the presence of TiO_2/rGO particles. This morphological structure is beneficial for photocatalytic reaction in membrane filtration as the uniformly distributed nanoparticles on the membrane surface would provide a higher access for photon energy absorption. Cui et al. [54] also have successfully incorporated magnetic Fe_3O4 nanoparticles along with TiO2 photocatalyst to enhance the particle distribution on the membrane surface under magnetic field. Thus far, other advanced nanoparticles loading techniques had also been invented for the same intention, such as surface grafting, interfacial polymerization, layer-by-layer assembly, and surface deposition [11,12,55]. The PVA coated PVDF-TiO_2/rGO membrane surface presented in Fig. 7(c) has smooth surface with minimum surface defect. It was likely due to the presence of PVA layer that repairs the surface defect. Similar observations were also reported by previous study where PVA coating improves membrane surface morphology [24,56]. Fig. 7(d),(e),(f) show cross-section SEM images of neat PVDF, PVDF-TiO_2/rGO nanohybrid membrane, and PVA coated PVDF-TiO_2/rGO, respectively. SEM images have displayed the existence of macrovoid and porous finger-like structure of all fabricated membranes. Overall, the cross-section image of the membranes show a quite similar morphological structure of finger-like voids. However, the TiO_2/rGO incorporated membranes exhibited larger finger-like macrovoids. It could be due to the effect of

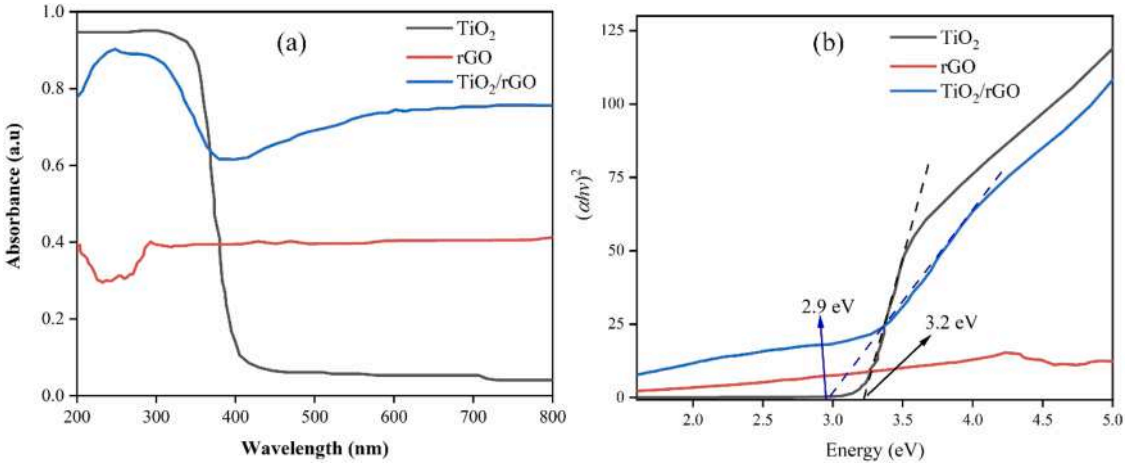

Fig. 5. (a) UV-Vis diffuse reflectance spectra (DRS) and (b) the Tauc's plot of prepared materials for band gap energy determination.

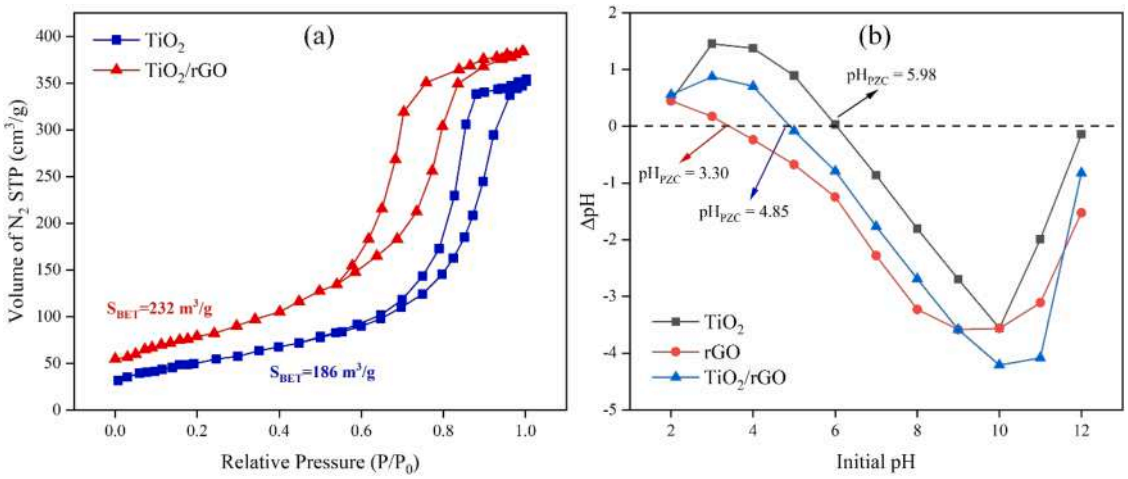

Fig. 6. (a) N_2 adsorption-desorption isotherms BET hysteresis loop (b) plot for pH_{PZC} determination of synthesized materials.

the hydrophilic TiO_2 and rGO loading into PVDF casting solution that increased the hydrophilicity that subsequently alters the thermodynamic instability and low rheological properties, thereby enhancing the solvent-water exchange rate during phase inversion leaving large finger-like macrovoids [57]. A previous study found that macrovoids might be formed when the viscosity of the casting solution was high and induced sudden-collapsed of finger-like structures formation [58]. Theoretically, larger finger-like macrovoids can be correlated with higher water permeability due to low kinetic hindrance. Interestingly, the cross-section morphology of PVA coated membranes has a thicker and denser top skin layer due to the cross-linked PVA polymer application. The dense skin layer of the membrane is responsible for providing a higher layer selectivity. With massive hydroxyl group of PVA polymer chain, the PVA coated membrane is expected to have superhydrophilic surface to create hydration layer that enhances membrane's water permeability and antifouling properties.

3.2.2. *Membrane porosity and pore size properties*

Porosity is one of the imperative parameters that determines membrane's physical characteristics and filtration performance. Table 3 shows the porosity and pore size of the fabricated membranes. Practically, both characteristics are closely related to the membrane morphology, especially on its surface. In general, porosity strongly affects membrane performances, especially its flux and rejection against pollutants. Based on the data tabulated in Table 3, the porosity of the neat PVDF membrane is the lowest (33.85%). This value is in good agreement with its SEM result that the finger-like structure of this membrane is very narrow. As expected, the porosity of the PVDF membrane increased with the incorporation of TiO_2, rGO, and TiO_2/rGO nanoparticles. This increase in porosity could be due to the formation of larger microvoids as evidenced by the SEM images (Fig. 7) as the result of thermodynamic instability change upon the addition of nanoparticles. Another possible reason is that the nanoparticles loading created gaps in the polymer matrix, thus the more cavities are developed with the increasing amount of nanoparticles which leads to a higher porosity. It confirms the SEM results in Fig. 7 where the addition of hydrophilic nanoparticles caused the membrane becomes more porous.

The cross-linked PVA coating on the PVDF-TiO_2/rGO membrane caused a decrease of membrane porosity up to 57.23% compared with that of uncoated PVDF-TiO_2/rGO membrane. This decrease was the results of the penetration of PVA solution into membrane surface pores that filled-up the void fraction of surface pores [59]. It confirms the SEM results in Fig. 7 that modification by cross-linked PVA coating produced a smooth surface which leads to the reduction of pore volume. The estimated membrane pore size obtained from Guerout-Elford-Ferry equation showed that the average pore size of fabricated membranes was around 2–3 nm. This finding suggests that the fabricated membranes are in the transition of nanofiltration and ultrafiltration region or classified as tight ultrafiltration (TUF) membrane with MWCO range of 300 – 5000 Da [60]. This type of pressure driven membrane is prospective for dyes and polyvalent salts removal in the textile wastewater treatment application according to previous study [61].

3.2.3. *FTIR spectra of the fabricated membranes*

Functional groups alteration of the fabricated membranes was identified using FTIR spectrophotometry over a frequency range of 4000 – 450 cm^{-1}. The FTIR spectra of all fabricated membranes are shown in Fig. 8. Visually, the FTIR spectra of membranes are of similar pattern with consistent peak belongs to polyvinylidene fluoride molecule. The typical peaks of PVDF are 840 cm^{-1}, 1177 cm^{-1}, and 1400 cm^{-1} that can be assigned to the alkyl halide R-F or C-F stretching, the C-C stretching of polymer backbone, and alkanes C-H stretching, respectively [62]. It proves that the spectrum of the composite membrane can sustain the absorption peak characteristics of neat PVDF membranes. Both peaks at 1177 cm^{-1} and 840 cm^{-1} indicated the existence of the C-F functional group. Meanwhile, peaks of 1400 cm^{-1} represented the asymmetric and symmetrical vibrations of the CH_2 functional group of PVDF membrane.

Basically, there was no significant difference in the FTIR spectrum when either TiO_2 or rGO nanoparticles were added to the PVDF membrane. However, weak broad peak appeared at 3347 cm^{-1} in the PVDF-TiO_2 membrane which can be attributed to the OH vibration of absorbed H_2O on the TiO_2 surface. The C-F stretching peak of PVDF-TiO_2 was shifted from 1177 to 1073 cm^{-1} which might be due to the interaction of fluoride with TiO_2. Moreover, when rGO nanoparticles were added, new peak appeared in the FTIR spectra, which was 1022 cm^{-1} in the PVDF-rGO, PVDF-rGO/TiO_2. A weak peak at 1022 cm^{-1} might be generated due to the vibration of the C-O-H functional group [63]. Oxygen-containing groups in the rGO nanoparticles cause these three absorption bands. It confirmed that rGO was embedded in the composite membrane.

A previous research reported that modifying of a composite membrane with UV irradiation and PVA coating increased membrane's hydrophilicity [64]. As seen in the FTIR spectrum of the PVA coated membrane, a strong wide peak appears between 3567 and 3130 cm^{-1}. This fact indicates an increase in the OH group due to the addition of PVA [64]. Additionally, this result also confirmed the successful PVA coating process on the PVSDF-TiO_2/rGO membrane surface. Fig. 9 illustrates the interaction of PVA polymer and PVDF polymer with the presence of TiO_2 nanoparticles. PVA was applied onto PVDF membrane surface via dip-coating and followed by crosslinking process using glutaraldehyde. PVA chain was crosslinked via esterification reaction of

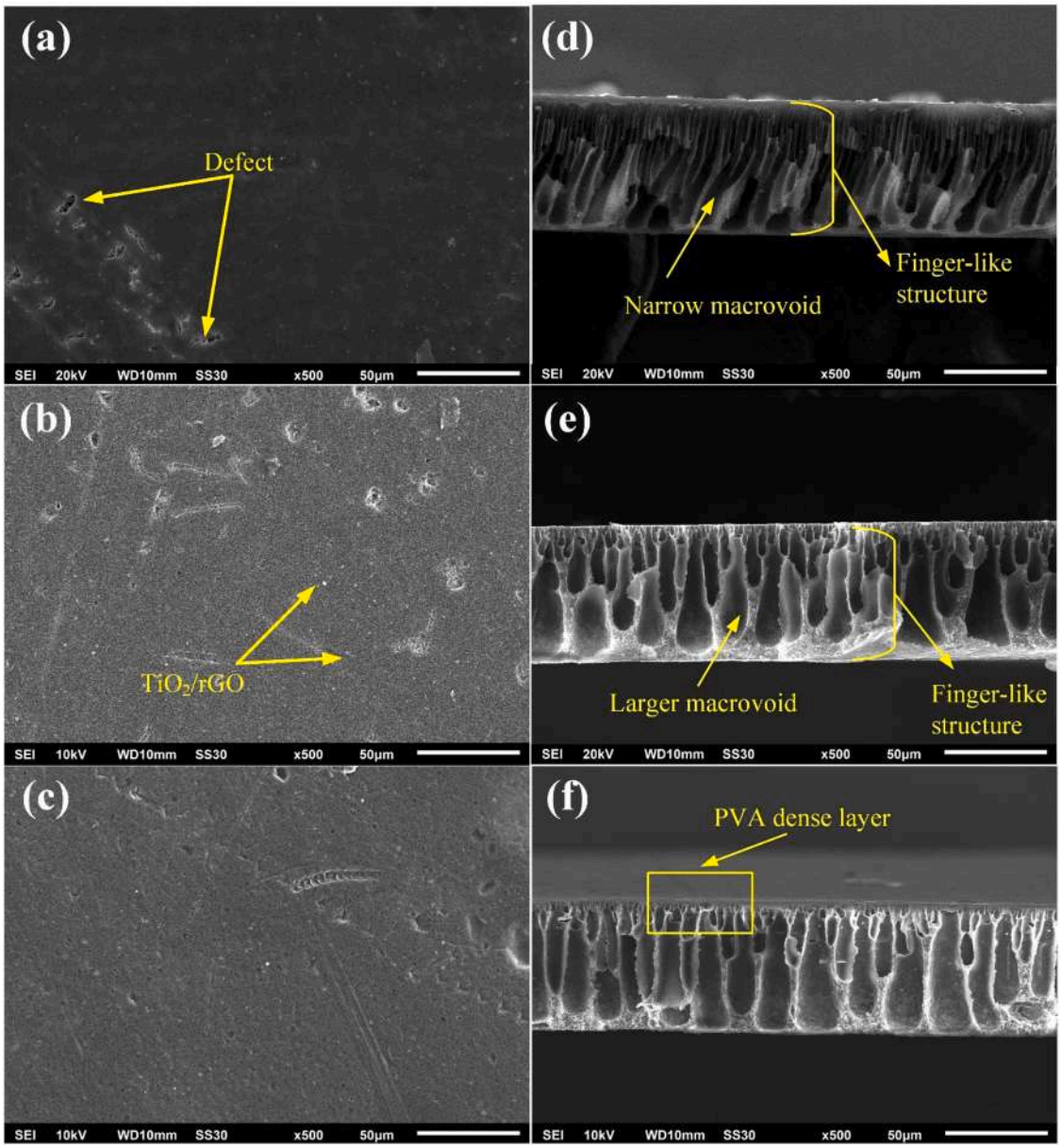

Fig. 7. (a), (b), (c) Surface SEM images of neat PVDF membrane, PVDF-TiO_2/rGO, and PVA coated PVDF-TiO_2/rGO, respectively. (d), (e), (f) cross-section SEM images of neat PVDF membrane, PVDF-TiO_2/rGO, and PVA coated PVDF-TiO_2/rGO, respectively.

Table 3
Porosity and pore size of the fabricated membrane.

Membranes	Porosity (%)	Estimated Pore size radius (nm)
Neat PVDF	33.85 ± 2.76	3.83 ± 0.31
PVDF–TiO_2	44.71 ± 2.37	3.13 ± 0.29
PVDF–rGO	83.76 ± 3.82	2.15 ± 0.38
PVDF-TiO_2/rGO	83.98 ± 1.79	2.14 ± 0.09
PVDF-TiO_2/rGO + PVA	57.23 ± 3.37	2.77 ± 0.30

carboxyl group of GA and hydroxyl group of PVA, resulting in the formation of ester bridge group network. This network prevented PVA polymer to swell during filtration process. Moreover, the interaction of PVA layer with PVDF was an intermolecular force between Hydrogen of hydroxyl group in PVA with Fluoride in PVDF. Hydrogen and fluoride have large difference in electronegativity value ($\Delta\chi$=2.0) which potentially to form dipole-dipole interaction (hydrogen bond). The incorporation of TiO_2/rGO into PVDF membrane also increase the interaction between PVA and PVDF membrane by providing O-Ti-O group to interact with hydrogen in hydroxyl group of PVA. In the other part, Ti has dipole-dipole interaction with fluoride due to its large electronegativity gap ($\Delta\chi$=2.66). It suggests that TiO_2/rGO has excellent chemical compatibility with PVDF and PVA.

3.2.4. Membrane wettability: surface hydrohilicity, water uptake, surface energy

Hydrophilicity is one of the fundamental factors that affect membrane performance, especially membrane permeability and membrane fouling tendency. To find out the hydrophilicity of the membrane based on the water contact angle, the sessile-drop method was performed. Fundamentally, a smaller value of water contact angle indicates a higher hydrophilicity of the membrane and vice versa. Fig. 10(a) shows the water contact angle of the neat and modified PVDF membranes. Modification of the PVDF membrane with the addition of TiO_2 and rGO nanoparticles have successfully enhanced surface hydrophilicity of the membranes. However, the sole incorporation of rGO as nanoparticle

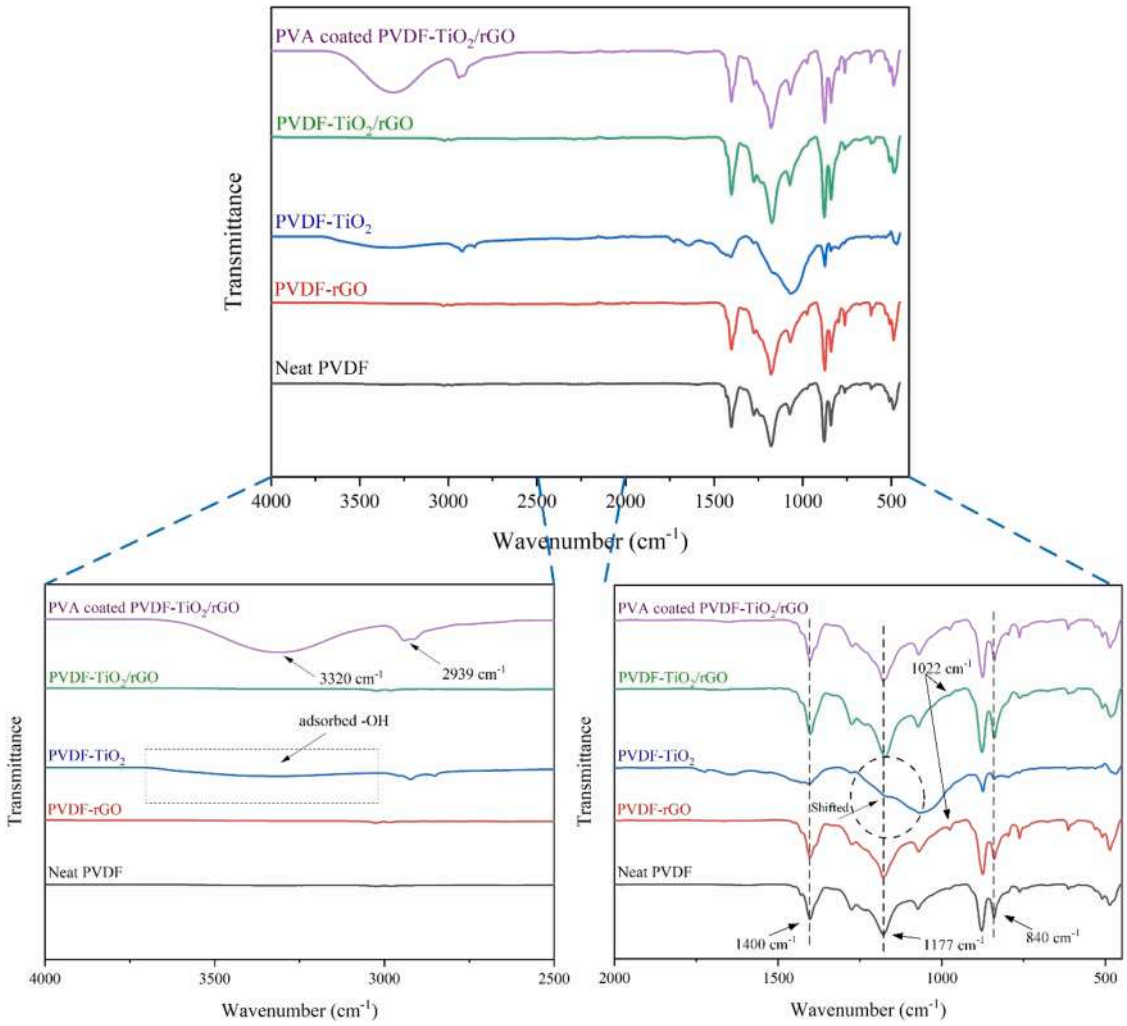

Fig. 8. FTIR spectra of fabricated membranes.

fillers in PVDF membrane did not considerably improve membrane's surface hydrophilicity. On the other hand, the addition of 2.5 wt% of rGO slightly decreased water contact angle from 68.5 to 68º. This observation is likely due to the poor oxygen containing site of rGO after reduction process.

Surprisingly, the addition of 1.5 wt% TiO_2 and TiO_2/rGO nanoparticles reduced the water contact angle until 65.83° and 65.5º, respectively. From the fundamental perspective, the improvement of surface hydrophilicity of the membrane is contributed by the presence of TiO_2. A similar observation was also reported by Lou et al. [62] where the addition of hydrophilic additives such as rGO/TiO_2 nanoparticles could increase the hydrophilic properties by providing oxygen-containing groups such as Ti-O. The addition of hydrophilic nanoparticles has also been reported to increase the surface roughness of the membrane that facilitates better contact between water molecules and OH groups and improves diffusion through the membrane surface. However, upon addition of TiO_2/rGO nanoparticles, the contact angle value was not significantly different from the PVDF-TiO_2 membrane with a contact angle of 65.83°. This phenomenon is plausible because the rGO nanoparticles used in this work was prepared by GO reduction process, which leads to a lower OH content in rGO [34]. Therefore, the addition of rGO to the membrane did not significantly increase the hydrophilicity compared to that of TiO_2 nanoparticles addition. Although no significant effect was obtained, the addition of rGO/TiO_2 combined particles successfully enhanced the PVDF membrane's hydrophilicity, which is one of the efforts to reduce fouling on the membrane. Surprisingly, the PVA coated membrane exhibits the lowest water contact angle (53.03º). As evidenced by FTIR analysis in the earlier section, the PVA coated membrane has more hydroxyl groups from PVA polymer which causes a more pivotal dipole-dipole interaction between cross-linked PVA and water molecules. Water uptake ability of membrane can be indirectly correlated with water contact angle. It describes membrane porosity and affinity towards water molecules. The water uptake of fabricated membranes were 40.25%, 53.33%, 54.21%, 54.83%, and 63.20% for the neat PVDF, PVDF-rGO, PVDF-TiO_2, PVDF-TiO_2/rGO, and PVA coated PVDF-TiO_2/rGO membranes, respectively. The nanohybrid PVDF showed a higher water uptake ability compared with that of neat PVDF. This higher water sorption ability is supported by a higher porosity and larger macrovoid as proven by the SEM images and porosity values. This intense water sorption ability can also be helpful in enhancing the membrane's permeability. The neat PVDF membrane has the lowest surface energy (γ_s) with the portion polar surface energy (γ_s^p) is lower than that of dispersive surface energy (γ_s^d). It reveals that naturally PVDF has low affinity towards polar substance such as water molecule. The PVDF-TiO_2/rGO membrane with PVA coating has shown the highest surface energy with higher portion of polar surface energy. These characterizations have revealed a successful modification of improving membrane surface hydrophilicity and wettability, which resulted in an improved permeability and antifouling properties.

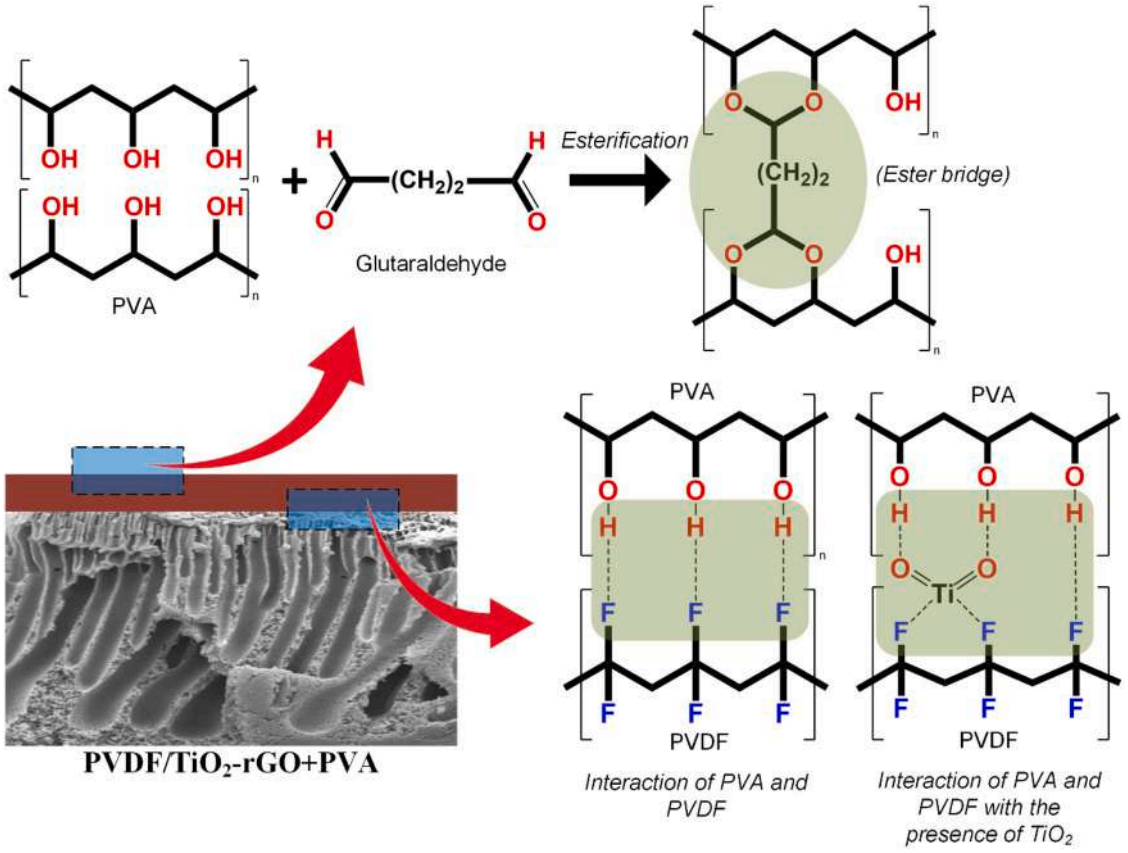

Fig. 9. Illustration of PVA and PVDF-TiO_2/rGO interaction.

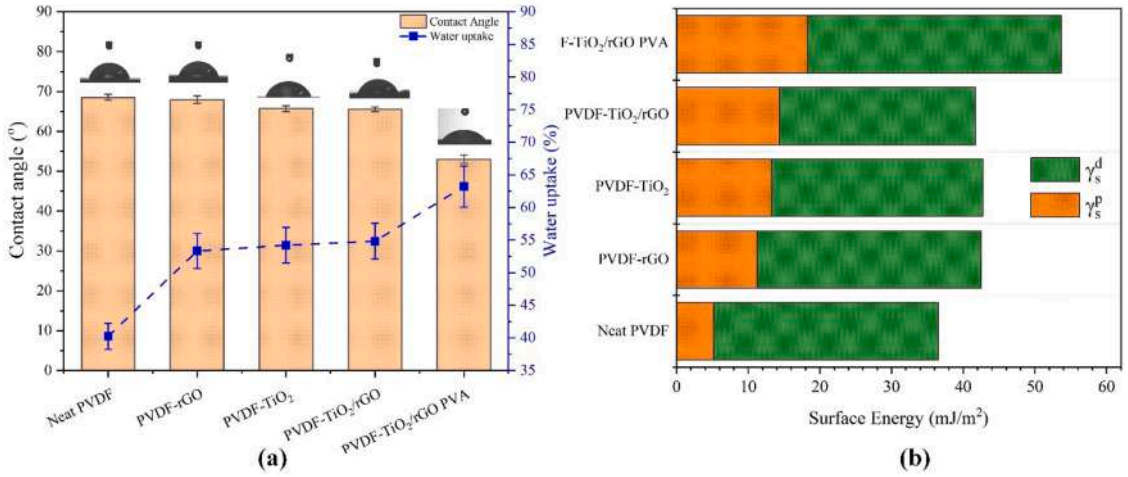

Fig. 10. Membrane surface properties (a) water contact angle and water uptake, (b) surface energy (γ_s).

3.2.5. Electron dispersive X-Ray (EDX) analysis of fabricated membranes

An EDX analysis of the fabricated membranes was conducted to ensure the presence of the nanoparticles added to the casting solution because the nanoparticles in the casting solution might leach out during phase inversion process. The elemental and oxide composition of the tested membranes (PVDF-TiO_2/rGO 2 wt%) is shown in Table 4. The membrane is composed of 44.37% of carbon and 53.80% of floride indicating both substances are the main constituents of PVDF polymer. The mass percentage of TiO_2 was found to be 1.83 wt%, which is smaller than its expected content in the membrane due to the leaching of TiO_2 nanoparticles during the phase inversion [65]. However, the TiO_2 content in PVDF-TiO_2/rGO membrane was higher than that of PVDF-TiO_2 membrane (1.20 wt%). This observation might be due to the improved the nanoparticle affinity with PVDF polymer through van der Waals interaction caused by the presence of rGO. The uniform dispersion of photocatalysts on the membrane surface has prevented particles aggregation and release.

3.3. Performance evaluation in Batik Wastewater treatment

3.3.1. Effect of TiO_2 loading on membrane performance

The addition of TiO_2 nanoparticles to the membrane was expected to

Table 4
Elemental and oxide composition of PVDF-TiO_2/rGO using EDX analysis.

Element	Mass (%)		Compound	Mass (%)	
	PVDF-TiO_2	PVDF-TiO_2/rGO		PVDF-TiO_2	PVDF-TiO_2/rGO
Carbon (C)	48.15	44.37	Carbon (C)	48.15	44.37
Oxygen (O)	0.48	0.37	Fluoride	50.65	52.18
Fluoride	50.65	53.80	(F)	1.20	1.83
(F)	0.72	1.10	TiO_2		
Titanium (Ti)					
Total	100	100		100	100

influence membrane's permeability and selectivity. A successful result can be observed based on membrane performance evaluations presented in Fig. 11, which focuses on the permeate flux and ability to reject contaminants during Batik wastewater treatment. Fig. 11(a) shows that the PVDF membrane with 1.5 wt% TiO_2 has the highest and most stable flux value compared to the other prepared membranes. The initial flux was 22.36 $L.m^{-2}h^{-1}$, but it continuously decreased until 13.15 $L.m^{-2}h^{-1}$ in the last 180 min. Meanwhile, the PVDF with 2.0 wt% of TiO_2 loading exhibited the lowest flux value of ~13.15 $L.m^{-2}h^{-1}$ in the first 30 min to ~9.87 $L.m^{-2}h^{-1}$ in the last 180 min. The reason behind this flux enhancement is due to the high affinity of TiO_2 towards water, which improved water penetration rate into the membrane during the coagulation stage of the phase inversion process. The presence of TiO_2 also caused the enhancement of water-solvent interdiffusion rate leading to the formation of a more porous membrane. Based on the membrane porosity test (Table 3) and SEM images (Fig. 7), it is confirmed that TiO_2 embedded membrane visually has a larger macrovoids. Water-soluble NMPs exited the membrane during the coagulation stage, while TiO2 particles remained in the membrane matrix and clogged some membrane pores. This process can also be affected by particle aggregation phenomenon. For this reason, the addition of different amounts of TiO_2 results in different structures.

Rejection analysis was conducted to measure pollutant parameters in wastewater to evaluate pollutant removal capacity of the membrane. As seen in Fig. 11(b), the COD rejection fluctuates along with the increasing of TiO_2 loading concentration. 1.5 wt% of TiO_2 have increased the COD rejection from 65% to 80%. COD level in wastewater is associated with the presence of natural organic matter (NOM) in water. The improved rejection rate of COD could be attributed to the photodegradation with the presence of TiO_2. Previous study indicated the ability of TiO_2 in NOM mineralization at low concentration under UV irradiation [66]. However, further increasing of TiO2 concentration has significantly decreased the COD removal down to 25% after the loading of 2.5 wt% TiO_2. This COD rejection decline could be due to TiO_2 over-loading that initiates nanoparticle aggregation. The nanoparticle aggregation has been reported as the cause of unselective voids formation. Similar trend was also shown by TDS rejection and dyes rejection. The pore size estimation has indicated that this membrane type is unable to reject free monovalent ions. The rejected TDS might be the ionic dyes and acids such as azo, anthraquinone, nitroso, remazol etc. It is supported by similar trend and level of TDS rejection and dyes rejection.

3.3.2. *Effect of TiO/rGO nanocomposite loading on membrane performance*

The photocatalyst nanocomposite of TiO_2 and rGO was prepared using an equal mass ratio for both TiO_2 and rGO. Fig. 12 shows the effect of loading concentration on the membrane performance for Batik wastewater treatment was evaluated based on the permeate flux and pollutants rejection. Fig. 12(a) shows that the 2.5 wt% TiO_2/rGO loading in PVDF membrane had the highest and most stable flux, which is 24.99 $L.m^{-2}h^{-1}$ in the first 30 min and continuously decreased to 19.07 $L.m^{-2}h^{-1}$ in the last 30 min. The interaction of rGO with TiO_2 improved the electron transform from CB of TiO_2 to rGO nanosheets, which subsequently reduced the charge recombination and enhanced the photocatalytic activity. The increased photoactivity generated more reactive oxygen species (ROS) that attracts water molecules. Another reason is that the combination of TiO_2 and rGO synergistically increased the surface hydrophilicity, water uptake, and polar surface energy thus enhancing membrane's water permeability.

According to Fig. 12(b), the COD rejection was significantly increased with the increasing of TiO_2/rGO nanocomposite loading. The COD rejection by the neat PVDF was 65% and it was enhanced up to 75% upon the addition of 2.5 wt% of TiO_2/rGO. Nevertheless, the variation of TiO_2/rGO nanocomposite concentration showed insignificant change in TDS rejection where all membranes have comparable rejection rate around 80%. The highest dyes rejection of Batik wastewater was achieved by membrane with 2.0 wt% of TiO_2/rGO at rejection value of 87.79%. Es expected, both COD and dyes rejection have similar trend because these contaminants are organic compounds. When the filtration was carried out under UV irradiation, the presence of TiO_2/rGO photocatalyst promoted the generation of ROS leading on organic degradation. Therefore, the simultaneous process of molecular exclusion by membrane and photodegradation has improved the overall rejection efficiency. Despite the prepared membranes have pore size radius in the range of TUF (2–3 nm), the TDS rejection was relatively high for all membranes. This results could be due to the solutes rejection via Gibbs-Donnan exclusion mechanism where solutes were rejected based on their surface charge. The PZC characterization has shown that both TiO_2 and rGO nanoparticles are positively charged particles in solution with

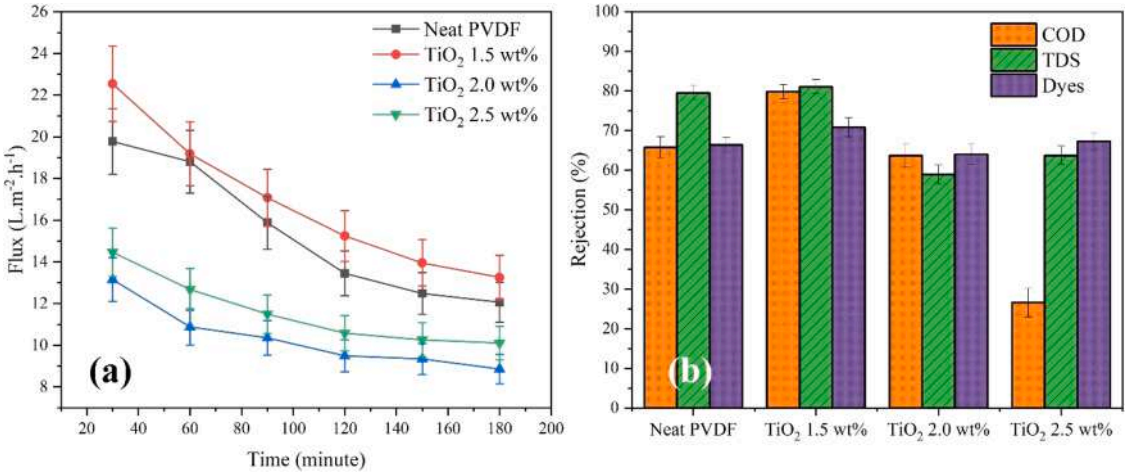

Fig. 11. Effect of different TiO_2 loadings on (a) Permeate flux and (b) Pollutant rejection.

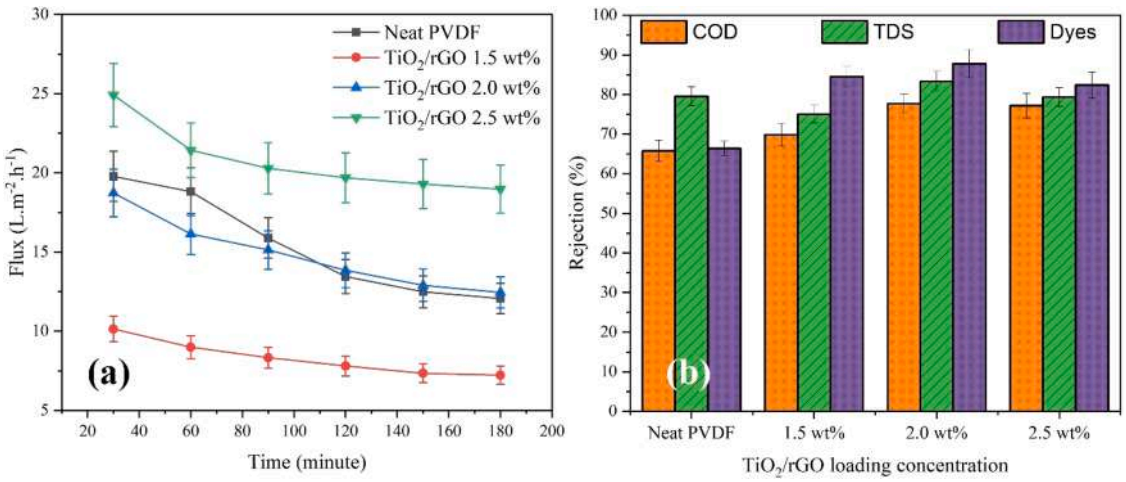

Fig. 12. Membrane performance in Batik wastewater treatment at various TiO_2/rGO nanocomposite loading concentration (a) permeate flux and (b) pollutants rejection.

pH > 6. The pH of Batik wastewater was 6.9, thus the membrane surface was protonized to form positive charged layer with strong ability to reject cations. The performance evaluation also showed that the COD rejection efficiency was relatively lower than the rejection of other two parameters. This observation is possible because the ionization of oxygen-containing groups can still have the opportunity to attract organic molecules via intermolecular forces. Therefore, some pollutants can wriggle out during filtration [34]. Meanwhile, the increased dye rejection after the addition of rGO nanoparticles in the membrane was due to the adsorption of dye molecules by membrane surface and influence the membrane flux via physical and chemical interactions, such as hydrophobic interactions dipole forces, and charge transfer (hydrogen bonds). In addition, the dye molecules have amino, sulfonate, and hydroxyl groups as active species attached to the aromatic ring, resulting in an interfacial force between the dye and the membrane, which has carboxyl, amide, and amino functional groups. Finally, these interactions resulted in a high rejection value of the color substances [67]. Based on this study, the TiO_2/rGO loading at 2.0 wt% has shown the best performance by reaching the highest pollutants rejection with moderate permeate flux value.

3.3.3. *Effect of cross-linked PVA coating on membrane performance*

The evaluation of PVA coating influence on the photocatalytic membrane performance was carried out using PVDF-TiO_2/rGO 2.0 wt% and followed by PVA coating with different concentration (2 and 4 wt %). The PVA coated membrane was crosslinked using glutaraldehyde to avoid membrane swelling during filtration process. Based on the permeate flux and solutes rejection evaluation in Batik wastewater treatment, a performance enhancement was observed. The flux profile and contaminants rejection rates are shown in Fig. 13.

As shown in Fig. 13(a), the PVA coating on membrane surface at low concentration (2 wt%) slightly enhanced the permeate flux by providing initial flux increment from 18.9 $L.m^{-2}h^{-1}$ to 19.5 $L.m^{-2}h^{-1}$. This improvement is contributed by hydrophilic layer of PVA polymer that forms hydration layer leading on higher water permeability. In contrast, 4 wt% PVA coating on membrane surface significantly decreased the permeate flux down to 9.4 $L.m^{-2}h^{-1}$. This flux decline could be due to the higher polymer density that hinder the penetration of water molecules to pass through membrane barrier. This reason is supported by the SEM cross-section images of the PVA coated membrane where its skin layer was thicker than that of uncoated one. Furthermore, the porosity characterization also showed the PVA coated membrane had a lower porosity that that of uncoated membrane. Based on this study, the PVA concentration as a coating agent for membrane surface to enhance water permeation should not exceed 4 wt%.

The PVA coating on membrane surface positively affected the solutes rejection. The solutes rejection increased along with the increasing of PVA concentration. There are two possible reasons that support this

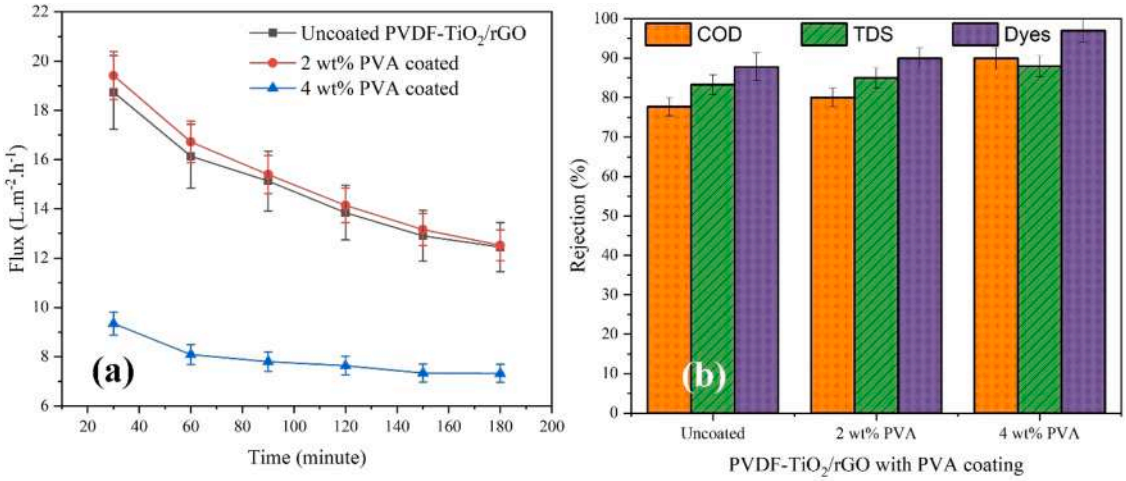

Fig. 13. Membrane performance in Batik wastewater treatment at various PVA concentration as coating agent (a) permeate flux and (b) pollutants rejection.

rejection enhancement. First, the supplementation of the membrane matrix with TiO_2/rGO synergistically increased the photoactivity under UV light. According to Xu et al. [68], PVDF–rGO membranes exhibited a closely similar photocatalytic properties to PVDF–TiO_2 membranes. It indicates that rGO has a similar characteristic with semiconductor as photocatalyst and that it has a similar band-gap energy to TiO_2. The integration of TiO_2 and rGO in the PVDF membrane is beneficial for decreasing the effect of charge recombination and ultimately increasing photocatalytic efficiency. Under UV irradiation, electron in VB of TiO_2 can be excited to produce photo-electrons (e^-) and holes (h^+). These electrons are then transferred to the rGO nanosheets that possess charge transfer ability. The electron can be captured by oxygen molecules (O_2) on the surface of TiO_2/rGO to produce O^{2-}, HO^{2-}, H_2O^{2-} and hydroxyl radicals (OH). These holes can interact with water molecules and hydroxyl groups (OH^-) to produce hydroxyl radicals OH. OH can degrade most complex organic compounds. According to Xu et al. [68], the photodegradation of organic substances occurs in two steps: firstly, the degradation of organic molecules into small fragments, and secondly, the mineralization of small organic fragments into inorganic molecules. The efficient photocatalytic properties have a beneficial effect in reducing membrane fouling due to the photocatalytic oxidation of the impurities, which ensures that the modified membrane can maintain a high permeate flux for a longer time than traditional membranes. Second, the PVA coating on membrane surface formed selective skin layer by providing hydroxyl sites, thereby increasing the solutes rejection via charge exclusion mechanism.

Fig. 13(b) also shows that 4 wt% PVA coated PVDF-TiO_2/rGO membrane under UV irradiation has the highest rejection of COD, TDS and dyes up to 89%, 87%, and 95%, respectively. The membrane rejected dye compounds more effectively than that of COD and TDS due to the in-situ photocatalytic process. During photocatalysis, TiO_2/rGO nanoparticles formed hydroxyl radicals, which are responsible for the degradation dye molecules. The OH^- radical is a very strong oxidizing agent that can oxidize most dyes. The combination of TiO_2/rGO with PVA coating has obviously improved the performance of PVDF membranes in removing intense contaminations of Batik wastewater simultaneously through membrane filtration and photocatalytic degradation.

3.3.4. *Effect of adsorption using bentonite and ozonation as pre-treatment*

Batik wastewater was treated by a combination of adsorption using bentonite, ozonation, and membrane filtration. The pre-treatment through adsorption using bentonite and ozonation prior to membrane filtration aimed to reduce the level of organic content in Batik wastewater. The pollutants removal efficiencies of adsorption and ozonation processes are presented in Supplementary materials Fig. S1. The adsorption process using bentonite clay has removed COD, TDS, and dyes up to 24.38%, 4.28%, and 40.52%, respectively. The ozonation process has removed COD, TDS, and dyes up to 18.21%, 0%, and 38.72%. the Adsorption-ozonation process has achieved removal efficiency of 50.28%, 5.06%, and 68.21%. The adsorption-ozonation performance has shown moderate pollutant removal, thus it suggests that membrane separation as final treatment is required to achieve clean water standard. The study of integrated system performance was conducted by determining the flux profile and the influence of the Batik wastewater pretreatment process on the reduction of organic pollutant levels in the effluent measured using the TDS, COD, and dyes removal. The effect of pretreatment processes on membrane filtration performance is presented in Fig. 14.

Fig. 14(a) exhibits the significant effect of adsorption and ozone pretreatment processes of Batik wastewater on the flux performance during filtration using the fabricated membrane. The combination of adsorption and ozone pre-treatment processes reduced the organic load of wastewater prior to membrane treatment. This steps has been proven to significantly reduced membrane fouling growth rate and enhanced the permeate flux and stability. Although adsorption process as pretreatment did not significantly influence the permeate flux enhancement, but it gave a more stable flux than that of membrane filtration without pretreatment. The bentonite used as the adsorbent was montmorrilonite clay with strong sorption capacity towards organic molecules, especially the dye compounds. With a reduced organic content, the cake layer formation rate can be minimized thus resulted in a more stable flux. In contrast, the ozonation process as a pre-treatment step provided significant enhancement of the permate flux up to 20 $L.m^{-2}h^{-1}$. This is because ozone is a strong oxidant that mineralize organic compounds through either direct or indirect oxidation pathway [69]. The combination of adsorption and ozonation has successfully given the highest and stable permeate flux profile.

The pollutant rejection in the effluent by the combined process of bentonite adsorption-ozonation-membrane filtration pretreatment is shown in Fig. 14(b). Overall, rejections of the integrated filtration system were 95%; 86.52%; and 95% for COD, TDS, and dyes, respectively. As a control experiment, a membrane filtration without any pretreatment was performed and obtained the rejection of COD, TDS, and dyes were 78%, 84%, and 86%, respectively. Pretreatment through adsorption was carried out using bentonite clay, which is a low-cost aluminium phyllosilicate adsorbent. Bentonite particles provide a large adsorption surface area that can bind organic substances through van der Waals intermolecular intraction. This adsorption step successfully reduced the pollutant content in the permeate from the effluent filtration compared to that without adsorption pre-treatment. It is also evidenced by the flux profile, which is higher than filtration without pretreatment. Meanwhile, ozonation is well-known as organic

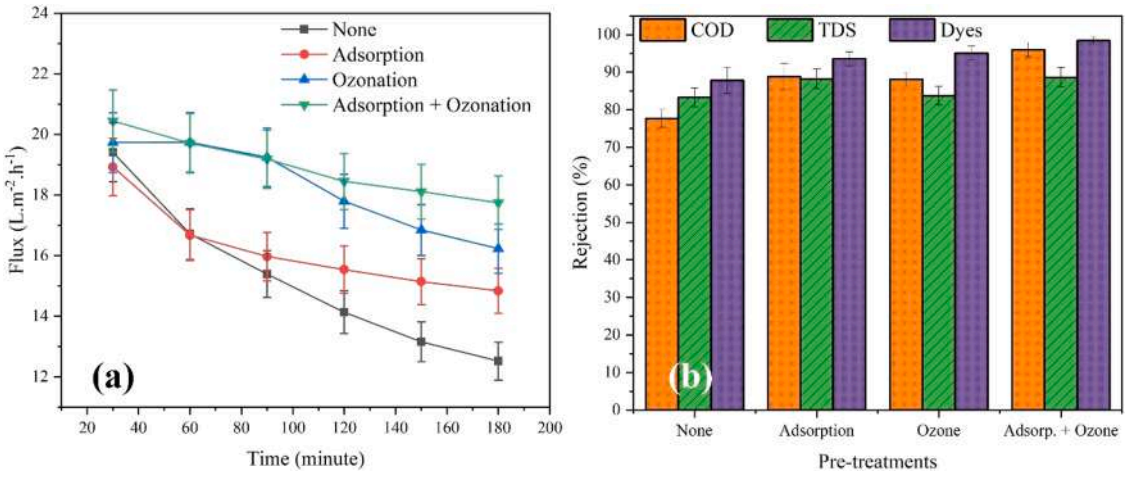

Fig. 14. Membrane filtration performance with different pre-treatment configuration in term of (a) Permeate flux (b) pollutants rejection performance.

degradation through an oxidation process. Oxidation reactions by ozone in water can occur when ozone forms the highly reactive hydroxyl radicals. Under this consideration, the oxidation rate will be faster at a higher hydroxyl (-OH) concentration in wastewater. In the ozone process, there is contact between ozone and waste pollutants; therefore, there is an oxidation process of organic compounds, which are the basis for the formation of dyes which will be oxidized to compounds with simpler molecular structures (mineralization). In the combined adsorption-ozone process, the adsorption process was carried out prior to ozonation because the adsorption process could withstand the large and complex organic contaminants. Hence, the remaining simpler organic compounds that escaped would then be degraded through the ozonation process.

3.4. Photocatalytic activity and kinetic evaluation of the fabricated membranes

Photocatalytic analysis of nanohybrid membranes was assayed by degrading the dye pollutant in Batik wastewater under UV C light irradiation. All fabricated membranes were tested for their photodegradation ability with control treatment of photo irradiation without photocatalytic membrane. The dyes degradation profile using photocatalytic membranes obtained from this investigation is presented in Fig. 15. Based on the results, it can be seen at the initial treatment, before the UV light was turned on, the pollutant removal was slightly influenced by the adsorption process of the nanohybrid membranes. However, the adsorption effect on the membranes is not significant compared to the overall pollutant removal by photocatalysis. The adsorption process by the membranes only achieved a maximum value of 10% of pollutant removal. After the UV lamp was turned on, the control experiment shows insignificant photodegradation where only a slight decrease of dyes concentration could be achieved due to the direct photolysis of dyes by UV C irradiation. Nevertheless, the effect of photolysis of dyes is so small and is not comparable to the pollutant removal by membrane's adsorption and photocatalysis. Similar results were also demonstrated by neat PVDF and PVDF-rGO membranes, which indicates that those membrane have no photocatalytic activity. This finding also reveals that rGO has no photocatalytic properties as evidenced by no band gap energy found in the DRS and Tauc's plot analysis. In contrast, PVDF-TiO_2, PVDF-TiO_2/rGO, and PVDF-TiO_2/rGO provided a strong dyes degradation up to ~90% for 120 min reaction. It is also found that PVDF-TiO2/rGO membrane exhibited a higher photodegradation activity than that of PVDF-TiO_2 membrane. The higher photodegradation of PVDF-TiO_2/rGO over PVDF-TiO_2 indicated the nanocomposite photocatalyst had superior photocatalytic activity. This is because TiO_2/rGO nanocomposite has 2.9 eV band gap energy which is lower than that of TiO_2 (3.2 eV). With a narrower band gap energy, the nanocomposite requires a lower photon energy to initiate the electron excitation for generating ROS around photocatalyst surface. Combination of TiO_2/rGO promotes rapid interfacial charge transfer and interfacial catalytic reaction [47]. rGO nanosheets can accept electrons to effectively separate electrons and holes, thus preventing the recombination center of e^-/h^+ pair as well as increasing photocatalytic efficiency.

To further study the photocatalytic activity on the membrane, the reaction kinetics of the organic compounds degradation was modeled following the zero order, Langmuir-Hinshelwood, and second order kinetic models, as the fitted results are depicted in Fig. 12(b-d),

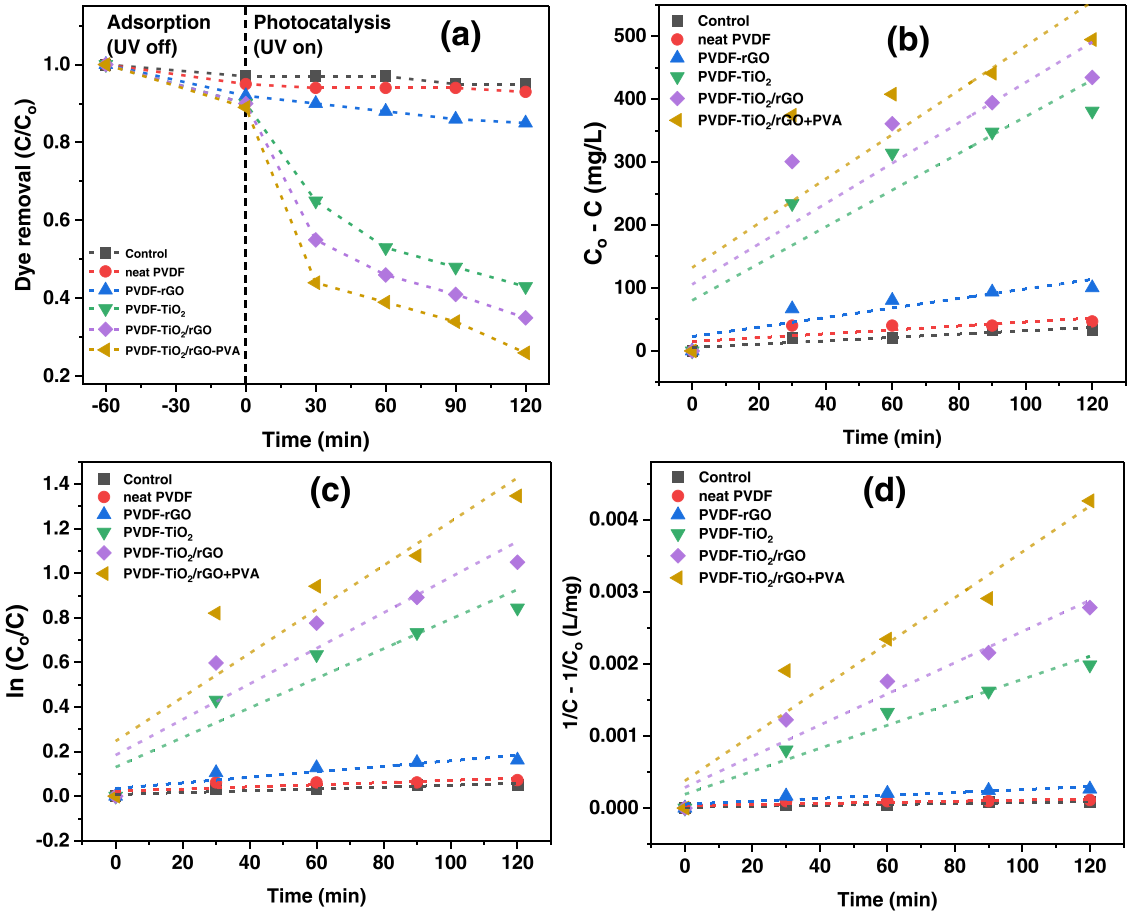

Fig. 15. (a) adsorption and photodegradation profiles of dyes using various membranes. Photodegradation kinetics fittings using several models: (b) zero order, (c) Langmuir-Hinshelwood, and (d) second order.

respectively. The estimated fitting parameters including the rate constants and coefficient of determination (R^2) can be seen in the Table S1. From the value of R^2, it is found that the photodegradation behavior is better fitted using the second order model. For example, the PVDF-TiO_2/rGO+PVA membrane the estimated R^2 values were 0.7175, 0.8457, and 0.9388 for zero order, Langmuir-Hinshelwood, and second order kinetic models, respectively. It is also found that the other membranes also showed relatively better R^2 in the second order model. The membranes with embedded active photocatalysts showed greater slope on all plots, which mean that they have higher rate constants compared to the other membranes with smaller slope. Higher rate constant on the kinetic equation represents faster photodegradation performance [70]. Furthermore, the photocatalytic activity on PVDF-TiO_2/rGO membrane was faster than PVDF-TiO_2 and PVDF-rGO membrane by increasing 30–100% of photocatalytic activity. This phenomenon can occur because of the synergistic effect between rGO and TiO_2 in the membrane, where rGO plays a role in increasing photon absorption on the membrane surface, leading to hydroxyl radicals (·OH) formation, thereby increasing photocatalytic activity [70].

3.5. Membrane fouling and stability evaluation

Fouling resistance is one of the simplest method in evaluating the fouling growth during membrane filtration process. In the raw wastewater sample from Batik textile industry, organic pollutants such as humus, wax, polyscharides, oil/grease, and dyes generally exist together. Therefore, the fouling resistance of different prepared membranes are performed to explore the influence of modification attempts on the fouling growth rate. The fouling resistance profile of all prepared membranes is presented in Fig. 16(a). As seen in Fig. 16(a), the total resistance of PVDF-rGO membrane was higher than that of neat PVDF membrane. The resistance was dominated by reversible fouling (cake layer). It could be due to the properties of rGO that possesses large surface area and ability to adsorp organic compounds on the membrane surface. Nevertheless, the irreversible fouling of PVDF-rGO membrane was significantly lower than that of neat PVDF membrane. The incorporation of TiO_2 and nanocomposite TiO_2/rGO to the membrane exhibited obvious fouling resistances reduction. It could be due to the in situ photodegradation and hydrophilicity enhancement thus promoting antifouling and self-cleaning properties. The lowest fouling resistance was achieved by PVA coated PVDF-TiO_2/rGO membrane. The modification of hydrophilic surface has significantly increased the antifouling properties of the membrane by decreasing the fouling resistance from 9.2×10^{11} m^{-1} to 5.1×10^{11} m^{-1}. Another parameter for assessing the performance of photocatalytic membrane is cycle test. The tested membrane was utilized to degrade dyes under UV irradiation after a predetermined reaction time, the membrane is cleaned and reused for photodegradation process. The results of five-consecutive cycle test of prepared membranes are depicted in Fig. 16(b). For the entire cycle experiment, the PVDF-TiO_2/rGO+PVA showed the highest photodegradation compared to other tested membranes. It is also found that in the next cycle experiments the PVA coated membrane successfully sustained the dyes degradation performance and experienced just a slight reduction in pollutant removal performance. The PVDF-TiO_2/rGO+PVA exhibited 73% pollutant degradation in the first cycle and 66% pollutant degradation in the fifth cycle, which shows a stable photodegradation activity. It could be due to the presence of PVA layer that form hydration layer thus preventing the attachment of organic pollutants on membrane surface that potentially retarded the UV light access for photocatalytic reaction.

4. Conclusion

This study has successfully manufactured PVA PVDF–TiO_2/rGO photocatalytic membrane and investigated its performance for Batik wastewater treatment. The combination of TiO_2 with rGO significantly reduced the band gap energy ~2.9 eV and promoted red shift light absorption at visible light region. The incorporation of inorganic fillers of rGO–TiO_2 to the membranes improved membrane performance and synergistically played their role as hydrophilic additives that resulted in the improvement of membrane morphology, permeability, and selectivity. Furthermore, the cross-linked PVA coating was found to provide an excellent antifouling characteristic of the membrane by enhancing membrane surface hydrophilicity that subsequently decrease the fouling resistance from 9.2×10^{11} m^{-1} to 5.1×10^{11} m^{-1}. The 2 wt% PVA coated PVDF–TiO_2/rGO membrane offers the best membrane performance with a permeate flux of 19.3 $L.m^{-2}.h^{-1}$, while the COD, TDS, and dyes rejections were 82.50%, 85%, and 90%, respectively. Moreover, the bentonite adsorption and ozonation as the wastewater pre-treatment steps had obviously enhanced the permeate flux up to 21 $L.m^{-2}.h^{-1}$ as well as increasing the pollutants rejection of 95%, 86.52%, and 95% for COD, TDS, and dyes, respectively. Finally, the improved photocatalytic activity of TiO_2/rGO nanocomposite, hydrophilicity enhancement by PVA coating have brought excellent antifouling and self-cleaning properties. The strategy of applying hydrophilic PVA on the membrane surface was to deal with reversible surface fouling while the photocatalyst inside the membrane was to deal with absorbed fouling. Therefore, both reversible and irreversible fouling can be minimized even with high load of contaminated wastewater. Overall, the results of this study provide insightful ideas for future applications of membranes

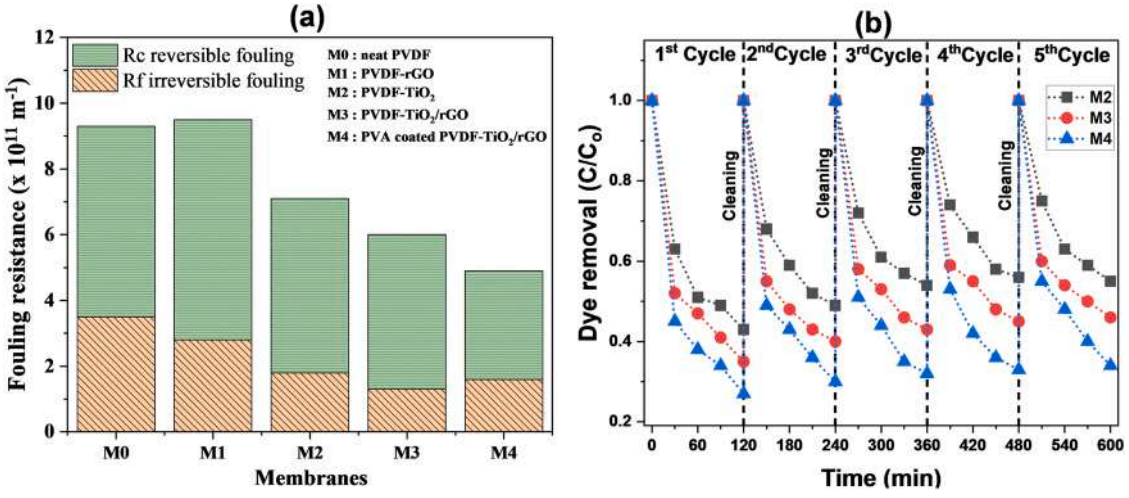

Fig. 16. (a) fouling resistance of membranes (b) Five consecutive cycles test of photocatalytic membranes for dyes removal under UV irradiation.

with prominent antifouling properties not only for Batik wastewater but also other highly polluted wastewater.

CRediT authorship contribution statement

Tutuk Djoko Kusworo: Resources, Methodology, Conceptualization, Validation, Writing – review & editing. **Andri Cahyo Kumoro**: Data interpretation, Writing – review & editing. **Nita Aryanti**: Data analysis, Validation. **Dani Puji Utomo**: Collecting data, Formal analysis. **Hasrinah Hasbullah**: Formal analysis, Writing – review editing. **Yasmin Nabilah**: Investigation, Collecting data, Writing – original draft. **Aufa Rasendriya**: Investigation, Collecting data, Writing – original draft. **Irvan**: Writing – original draft, Collecting data.

Declaration of Competing Interest

The authors declare that they have no known competing financial interests or personal relationships that could have appeared to influence the work reported in this paper.

Data availability

Data will be made available on request.

Acknowledgment

The authors acknowledged Institute for Research and Community Services (LPPM), Diponegoro University. This research was fully funded by Diponegoro University World-Class Research Grant (WCR-UNDIP) No. 118–31/UN7.6.1/PP/2022.

Appendix A. Supporting information

Supplementary data associated with this article can be found in the online version at doi:10.1016/j.jece.2022.108708.

References

[1] P.A. Permatasari and L. Cantoni, "Participatory Design to Create Digital Technologies for Batik Intangible Cultural Heritage: The Case of iWareBatik," in *Design, User Experience, and Usability: Design for Diversity, Well-being, and Social Development*, vol. 12780, M. M. Soares, E. Rosenzweig, and A. Marcus, Eds. Cham: Springer International Publishing, 2021, pp. 88–106. doi: 10.1007/978–3-030–78224-5_7.

[2] V. Jegatheesan, B.K. Pramanik, J. Chen, D. Navaratna, C.-Y. Chang, L. Shu, "Treatment of textile wastewater with membrane bioreactor: A critical review,", Biores. Technol. vol. 204 (2016) 202–212, https://doi.org/10.1016/j.biortech.2016.01.006.

[3] A. Mukimin, H. Vistanty, N. Zen, A. Purwanto, K.A. Wicaksono, "Performance of bioequalization-electrocatalytic integrated method for pollutants removal of hand-drawn batik wastewater,", J. Water Proc. Eng. vol. 21 (2018) 77–83, https://doi.org/10.1016/j.jwpe.2017.12.004.

[4] B.V. Tangahu, D.A. Ningsih, S.B. Kurniawan, M.F. Imron, "Study of BOD and COD Removal in Batik Wastewater using Scirpus grossus and Iris pseudacorus with Intermittent Exposure System,", J. Ecol. Eng. vol. 20 (5) (2019) 130–134, https://doi.org/10.12911/22998993/105357.

[5] K. Oginawati, Suharyanto Suharyanto, S.H. Susetyo, G. Sulung, Muhayatun Muhayatun, N. Chazanah, S.W. Dewi Kusumah, N. Fahimah, Investigation of dermal exposure to heavy metals (Cu, Zn, Ni, Al, Fe and Pb) in traditional batik industry workers, Heliyon vol. 8 (2) (2022), e08914, https://doi.org/10.1016/j.heliyon.2022.e08914.

[6] H. Rashidi, N.M.N. Sulaiman, N.A. Hashim, L. Bradford, H. Asgharnejad, M. M. Larijani, "Development of the ultra/nano filtration system for textile industry wastewater treatment,", Membr. Water Treat. vol. 11 (5) (2020) 333–344, https://doi.org/10.12989/MWT.2020.11.5.333.

[7] M. Laqbaqbi, M.C. García-Payo, M. Khayet, J. El Kharraz, M. Chaouch, "Application of direct contact membrane distillation for textile wastewater treatment and fouling study,", Sep. Pur. Technol. vol. 209 (2019) 815–825, https://doi.org/10.1016/j.seppur.2018.09.031.

[8] R. Lafi, L. Gzara, R.H. Lajimi, A. Hafiane, "Treatment of textile wastewater by a hybrid ultrafiltration/electrodialysis process,", Chem. Eng. Process., Process. Intensif. vol. 132 (2018) 105–113, https://doi.org/10.1016/j.cep.2018.08.010.

[9] A. Febriasari, Huriya, A.H. Ananto, M. Suhartini, S. Kartohardjono, "Polysulfone–polyvinyl pyrrolidone blend polymer composite membranes for batik industrial wastewater treatment,", Membranes vol. 11 (1) (2021) 66, https://doi.org/10.3390/membranes11010066.

[10] T.D. Kusworo, H. Susanto, N. Aryanti, N. Rokhati, I.N. Widiasa, H. Al-Aziz, D. P. Utomo, D. Masithoh, A.C. Kumoro, Preparation and characterization of photocatalytic PSf-TiO2/GO nanohybrid membrane for the degradation of organic contaminants in natural rubber wastewater, J. Environ. Chem. Eng. vol. 9 (2) (2021), 105066, https://doi.org/10.1016/j.jece.2021.105066.

[11] E. Jeong, J. Byun, B. Bayarkhuu, S.W. Hong, "Hydrophilic photocatalytic membrane via grafting conjugated polyelectrolyte for visible-light-driven biofouling control,", Appl. Catal., B vol. 282 (2021), 119587 https://doi.org/10.1016/j.apcatb.2020.119587.

[12] Y. Mi, N. Wang, X. Fang, J. Cao, M. Tao, Z. Cao, "Interfacial polymerization nanofiltration membrane with visible light photocatalytic self-cleaning performance by incorporation of CQD/TiO2,", Sep. Pur. Technol. vol. 277 (2021), 119500 https://doi.org/10.1016/j.seppur.2021.119500.

[13] J. Luo, W. Chen, H. Song, J. Liu, "Fabrication of hierarchical layer-by-layer membrane as the photocatalytic degradation of foulants and effective mitigation of membrane fouling for wastewater treatment,", Sci. Tot. Environ. vol. 699 (2020), 134398 https://doi.org/10.1016/j.scitotenv.2019.134398.

[14] R.R. Abdullah, K.M. Shabeed, A.B. Alzubaydi, Q.F. Alsalhy, "Novel photocatalytic polyether sulphone ultrafiltration (UF) membrane reinforced with oxygen-deficient Tungsten Oxide (WO2.89) for Congo red dye removal,", Chem. Eng. Res. Des. vol. 177 (2022) 526–540, https://doi.org/10.1016/j.cherd.2021.11.015.

[15] T.D. Kusworo, Budiyono, A.C. Kumoro, D.P. Utomo, "Photocatalytic nanohybrid membranes for highly efficient wastewater treatment: A comprehensive review,", J. Environ. Manag. vol. 317 (2022), 115357 https://doi.org/10.1016/j.jenvman.2022.115357.

[16] H.P. Ngang, B.S. Ooi, A.L. Ahmad, S.O. Lai, "Preparation of PVDF–TiO2 mixed-matrix membrane and its evaluation on dye adsorption and UV-cleaning properties,", Chem. Eng. J. vol. 197 (2012) 359–367, https://doi.org/10.1016/j.cej.2012.05.050.

[17] A. Piątkowska, M. Janus, K. Szymański, S. Mozia, "C-,N- and S-Doped TiO2 Photocatalysts: A Review,", Catalysts vol. 11 (1) (2021) 144, https://doi.org/10.3390/catal11010144.

[18] S. Haq, W. Rehman, M. Waseem, V. Meynen, S.U. Awan, A.R. Khan, S. Hussain, Zain-ul-Abdin, S.U. Din, M. Hafeez, N. Iqbal, Effect of Annealing Temperature on Structural Phase Transformations and Band Gap Reduction for Photocatalytic Activity of Mesopores TiO2 Nanocatalysts, J. Inorg. Organomet. Polym. vol. 31 (3) (2021) 1312–1322, https://doi.org/10.1007/s10904-020-01810-4.

[19] H. Fan, G. Yi, Z. Zhang, X. Zhang, P. Li, C. Zhang, L. Chen, Y. Zhang, Q. Sun, Binary TiO2/RGO photocatalyst for enhanced degradation of phenol and its application in underground coal gasification wastewater treatment, Opt. Mater. vol. 120 (2021), 111482, https://doi.org/10.1016/j.optmat.2021.111482.

[20] M. Shi, W. Li, Q. Wang, H. Xu, Y. Zhao, G. He, Q. Meng, H. Chen, One-step hydrothermal synthesis of BiVO4/TiO2/RGO composite with effective photocatalytic performance for the degradation of ciprofloxacin, Opt. Mater. vol. 122 (2021), 111726, https://doi.org/10.1016/j.optmat.2021.111726.

[21] J. Yu, Y. Zhang, J. Chen, L. Cui, W. Jing, "Solvothermal-induced assembly of 2D–2D rGO-TiO2 nanocomposite for the construction of nanochannel membrane,", J. Membr. Sci. vol. 600 (2020), 117870 https://doi.org/10.1016/j.memsci.2020.117870.

[22] I. Ratman, T.D. Kusworo, D.P. Utomo, D.A. Azizah, W.A. Ayodyasena, "Petroleum refinery wastewater treatment using three steps modified nanohybrid membrane coupled with ozonation as integrated pre-treatment,", J. Environ. Chem. Eng. vol. 8 (4) (2020), 103978 https://doi.org/10.1016/j.jece.2020.103978.

[23] S. Psaltou, A. Zouboulis, "Catalytic ozonation and membrane contactors—a review concerning fouling occurrence and pollutant removal,", Water vol. 12 (11) (2020) 2964, https://doi.org/10.3390/w12112964.

[24] T.D. Kusworo, A.C. Kumoro, D.P. Utomo, F.M. Kusumah, M.D. Pratiwi, "Performance of the Crosslinked PVA Coated PES-TiO2 Nano Hybrid Membrane for the Treatment of Pretreated Natural Rubber Wastewater Involving Sequential Adsorption – Ozonation Processes,", J. Environ. Chem. Eng. vol. 9 (2) (2021), 104855 https://doi.org/10.1016/j.jece.2020.104855.

[25] N. Rosman, W. Norharyati Wan Salleh, N. Aqilah Mohd Razali, S.Z. Nurain Ahmad, N. Hafiza Ismail, F. Aziz, Z. Harun, A. Fauzi Ismail, N. Yusof, Ibuprofen removal through photocatalytic filtration using antifouling PVDF- ZnO/Ag2CO3/Ag2O nanocomposite membrane, Mater. Today Proc. vol. 42 (2021) 69–74, https://doi.org/10.1016/j.matpr.2020.09.476.

[26] B. Li, I.S. Kim, S. Dai, M.N. Sarwar, X. Yang, "Heterogeneous Ag@ZnO nanorods decorated on polyacrylonitrile fiber membrane for enhancing the photocatalytic and antibacterial properties,", Colloid Interface Sci. Commun. vol. 45 (2021), 100543 https://doi.org/10.1016/j.colcom.2021.100543.

[27] H. Zhang, X. Quan, S. Chen, H. Zhao, Y. Zhao, "Fabrication of photocatalytic membrane and evaluation its efficiency in removal of organic pollutants from water,", Sep. Pur. Technol. vol. 50 (2) (2006) 147–155, https://doi.org/10.1016/j.seppur.2005.11.018.

[28] X. Li, L. Zhang, Z. Wang, S. Wu, J. Ma, "Facile fabrication of multiscale ZnO/cellulose composite membrane towards enhancing photocatalytic and mechanical properties,", Colloids Surf., A. vol. 636 (2022), 128156 https://doi.org/10.1016/j.colsurfa.2021.128156.

[29] A.L. Desa, N. Hairom, D. Sidik, N. Misdan, N. Yusof, M.K. Ahmad, A. W. Mohammad, A comparative study of ZnO-PVP and ZnO-PEG nanoparticles activity in membrane photocatalytic reactor (MPR) for industrial dye wastewater treatment under different membranes, J. Environ. Chem. Eng. vol. 7 (3) (2019), 103143, https://doi.org/10.1016/j.jece.2019.103143.

[30] H. Bai, X. Zan, L. Zhang, D.D. Sun, "Multi-functional CNT/ZnO/TiO2 nanocomposite membrane for concurrent filtration and photocatalytic degradation,", Sep. Pur. Technol. vol. 156 (2015) 922–930, https://doi.org/10.1016/j.seppur.2015.10.016.
[31] Y. Gao, M. Hu, B. Mi, "Membrane surface modification with TiO2–graphene oxide for enhanced photocatalytic performance,", J. Membr. Sci. vol. 455 (2014) 349–356, https://doi.org/10.1016/j.memsci.2014.01.011.
[32] H. Wang, J. Wang, X. Xiang, Y. Zhou, Q. Li, A. Tang, D. Liao, Y. Liu, H.B. Liu, Preparation of PVDF/CdS/Bi2WO6/ZnO hybrid membrane with enhanced visible-light photocatalytic activity for degrading nitrite in water, Environ. Res. vol. 191 (2020), 110036, https://doi.org/10.1016/j.envres.2020.110036.
[33] R. Molinari, M. Mungari, E. Drioli, A. Di Paola, V. Loddo, L. Palmisano, M. Schiavello, Study on a photocatalytic membrane reactor for water purification, Catal. Today vol. 55 (1–2) (2000) 71–78, https://doi.org/10.1016/S0920-5861(99)00227-8.
[34] T.D. Kusworo, A.C. Kumoro, N. Aryanti, D.P. Utomo, "Removal of organic pollutants from rubber wastewater using hydrophilic nanocomposite rGO-ZnO/PES hybrid membranes,", J. Environ. Chem. Eng. vol. 9 (6) (2021), 106421 https://doi.org/10.1016/j.jece.2021.106421.
[35] T.D. Kusworo, H. Susanto, N. Aryanti, N. Rokhati, I.N. Widiasa, H. Al-Aziz, D. P. Utomo, D. Masithoh, A.C. Kumoro, Preparation and characterization of photocatalytic PSf-TiO2/GO nanohybrid membrane for the degradation of organic contaminants in natural rubber wastewater, J. Environ. Chem. Eng. vol. 9 (2) (2021), 105066, https://doi.org/10.1016/j.jece.2021.105066.
[36] J.F. Leal, S.M.A. Cruz, B.T.A. Almeida, V.I. Esteves, P.A.A.P. Marques, E.B. H. Santos, "TiO $_2$ –rGO nanocomposite as an efficient catalyst to photodegrade formalin in aquaculture's waters, under solar light,", Environ. Sci.: Water Res. Technol. vol. 6 (4) (2020) 1018–1027, https://doi.org/10.1039/C9EW00950G.
[37] T.D. Kusworo, A.C. Kumoro, D.P. Utomo, F.M. Kusumah, M.D. Pratiwi, "Performance of the Crosslinked PVA Coated PES-TiO2 Nano Hybrid Membrane for the Treatment of Pretreated Natural Rubber Wastewater Involving Sequential Adsorption – Ozonation Processes,", J. Environ. Chem. Eng. vol. 9 (2) (2021), 104855 https://doi.org/10.1016/j.jece.2020.104855.
[38] T.D. Kusworo, F. Dalanta, N. Aryanti, N.H. Othman, "Intensifying separation and antifouling performance of PSf membrane incorporated by GO and ZnO nanoparticles for petroleum refinery wastewater treatment,", J. Water Proc. Eng. vol. 41 (2021), 102030 https://doi.org/10.1016/j.jwpe.2021.102030.
[39] F. Azeez, E. Al-Hetlani, M. Arafa, Y. Abdelmonem, A.A. Nazeer, M.O. Amin, M. Madkour, The effect of surface charge on photocatalytic degradation of methylene blue dye using chargeable titania nanoparticles,", Sci. Rep. vol. 8 (1) (2018) 7104, https://doi.org/10.1038/s41598-018-25673-5.
[40] T.D. Kusworo, N. Aryanti, Qudratun, D.P. Utomo, "Oilfield produced water treatment to clean water using integrated activated carbon-bentonite adsorbent and double stages membrane process,", Chem. Eng. J. vol. 347 (2018) 462–471, https://doi.org/10.1016/j.cej.2018.04.136.
[41] K. Al-Essa, "Activation of Jordanian Bentonite by Hydrochloric Acid and Its Potential for Olive Mill Wastewater Enhanced Treatment,", J. Chem. vol. 2018 (2018) 1–10, https://doi.org/10.1155/2018/8385692.
[42] N. Maximous, G. Nakhla, W. Wan, K. Wong, "Preparation, characterization and performance of Al2O3/PES membrane for wastewater filtration,", J. Membr. Sci. vol. 341 (1) (2009) 67–75, https://doi.org/10.1016/j.memsci.2009.05.040.
[43] H.T. Nguyen, S.-Y. Guo, S.-J. You, Y.-F. Wang, "Visible light driven photocatalytic coating of PAA plasma-grafted PVDF membrane by TiO_2 doped with lanthanum recovered from waste fluorescent powder,", 210144-0, Environ. Eng. Res. vol. 27 (3) (2022), https://doi.org/10.4491/eer.2021.144.
[44] D. Ayodhya, S. Perka, N. Nambigari, "Sunlight-driven efficient photocatalytic and antimicrobial studies of microwave-assisted Ir-doped TiO2 nanoparticles for environmental safety,", Nanochem. Res. vol. 3 (1) (2018) 36–49, https://doi.org/10.22036/ncr.2018.01.005.
[45] Y.-D. Zhou, Z.-Y. Zhao, "Interfacial structure and properties of TiO2 phase junction studied by DFT calculations,", Appl. Surf. Sci. vol. 485 (2019) 8–21, https://doi.org/10.1016/j.apsusc.2019.04.193.
[46] G.V. Khade, M.B. Suwarnkar, N.L. Gavade, K.M. Garadkar, "Green synthesis of TiO2 and its photocatalytic activity,", J. Mater. Sci: Mater. Electron vol. 26 (5) (2015) 3309–3315, https://doi.org/10.1007/s10854-015-2832-7.
[47] S. Prabakaran, K.D. Nisha, S. Harish, J. Archana, M. Navaneethan, "Yttrium incorporated TiO2/rGO nanocomposites as an efficient charge transfer layer with enhanced mobility and electrical conductivity,", J. Alloy. Compd. vol. 885 (2021), 160936 https://doi.org/10.1016/j.jallcom.2021.160936.
[48] X. Yu, Z. Li, K. Dang, Z. Zhang, L. Gao, L. Duan, Z. Jiang, J. Fan, P. Zhao, Enhanced photocatalytic activity of Ag–ZnO/RGO nanocomposites for removal of methylene blue, J. Mater. Sci: Mater. Electron vol. 29 (10) (2018) 8729–8737, https://doi.org/10.1007/s10854-018-8889-3.
[49] A.S. AlShammari, M.M. Halim, F.K. Yam, N.H.M. Kaus, "Synthesis of Titanium Dioxide (TiO2)/Reduced Graphene Oxide (rGO) thin film composite by spray pyrolysis technique and its physical properties,", Mater. Sci. Semicond. Process. vol. 116 (2020), 105140 https://doi.org/10.1016/j.mssp.2020.105140.
[50] B.S. Gonçalves, L. Silva, T. de Souza, V.G. de Castro, G.G. Silva, B.C. Silva, K. Krambrock, R.B. Soares, V. Lins, M. Houmard, E. Nunes, "Solvent effect on the structure and photocatalytic behavior of TiO $_2$ -RGO nanocomposites,", J. Mater. Res. vol. 34 (23) (2019) 3918–3930, https://doi.org/10.1557/jmr.2019.342.
[51] F.J. Sotomayor, K.A. Cychosz, M. Thommes, "Characterization of micro/mesoporous materials by physisorption: concepts and case studies,", Acc. Mater. Surf. Res. vol. 3 (2) (2018) 34–50.
[52] P. Kamedulski, M. Skorupska, P. Binkowski, W. Arendarska, A. Ilnicka, J. P. Lukaszewicz, "High surface area micro-mesoporous graphene for electrochemical applications,", Art. no. 1, Sci. Rep. vol. 11 (1) (2021) 22054, https://doi.org/10.1038/s41598-021-01154-0.
[53] M. Zeng, "Influence of TiO_2 Surface Properties on Water Pollution Treatment and Photocatalytic Activity,", Bull. Korean Chem. Soc. vol. 34 (3) (2013) 953–956, https://doi.org/10.5012/BKCS.2013.34.3.953.
[54] Y. Cui, J. Zheng, Z. Wang, B. Li, Y. Yan, M. Meng, "Magnetic induced fabrication of core-shell structure Fe3O4@TiO2 photocatalytic membrane: Enhancing photocatalytic degradation of tetracycline and antifouling performance,", J. Environ. Chem. Eng. vol. 9 (6) (2021), 106666 https://doi.org/10.1016/j.jece.2021.106666.
[55] X. Yan, L. Huo, C. Ma, J. Lu, "Layer-by-layer assembly of graphene oxide-TiO2 membranes for enhanced photocatalytic and self-cleaning performance,", Process Saf. Environ. Prot. vol. 130 (2019) 257–264, https://doi.org/10.1016/j.psep.2019.08.021.
[56] S.A. El-Behary, A.M. El-Aassar, M. Aboelfadl, N. Abdel-Atey, A.T. Kandil, "Surface modification of TFC membranes using PVA and nanomaterials for enhancing fouling resistance,", Des. Water Treat. vol. 193 (2020) 106–116, https://doi.org/10.5004/dwt.2020.25687.
[57] M. Han, "Thermodynamic and rheological variation in polysulfone solution by PVP and its effect in the preparation of phase inversion membrane,", J. Membr. Sci. vol. 202 (1–2) (2002) 55–61, https://doi.org/10.1016/S0376-7388(01)00718-9.
[58] M. Amirilargani, A. Sabetghadam, T. Mohammadi, "Polyethersulfone/polyacrylonitrile blend ultrafiltration membranes with different molecular weight of polyethylene glycol: preparation, morphology and antifouling properties: Polyethersulfone/ Polyacrylonitrile Blend UF Membranes,", Polym. Adv. Technol. vol. 23 (3) (2012) 398–407, https://doi.org/10.1002/pat.1888.
[59] M. Hidayah, T.D. Kusworo, H. Susanto, "Improving the Performance of Polysulfone-nano ZnO Membranes for Water Treatment in Oil Refinery with Modified UV Irradiation and Polyvinyl Alcohol,", Period. Polytech. Chem. Eng. vol. 66 (1) (2021) 43–53, https://doi.org/10.3311/PPch.17029.
[60] P.T.P. Aryanti, A.N. Hakim, S. Widodo, I.N. Widiasa, I.G. Wenten, "Prospect and challenges of tight ultrafiltration membrane in drinking water treatment,", IOP Conf. Ser.: Mater. Sci. Eng. vol. 395 (2018), 012012 https://doi.org/10.1088/1757-899X/395/1/012012.
[61] J. Lin, W. Ye, M.C. Baltaru, Y.P. Tang, N.J. Bernstein, P. Gao, S. Balta, M. Vlad, A. Volodin, A. Sotto, P. Luis, A.L. Zydney, B. Van der Bruggen, Tight ultrafiltration membranes for enhanced separation of dyes and Na2SO4 during textile wastewater treatment, J. Membr. Sci. vol. 514 (2016) 217–228, https://doi.org/10.1016/j.memsci.2016.04.057.
[62] L. Lou, R.J. Kendall, E. Smith, S.S. Ramkumar, "Functional PVDF/rGO/TiO2 nanofiber webs for the removal of oil from water,", Polymer vol. 186 (2020), 122028 https://doi.org/10.1016/j.polymer.2019.122028.
[63] W.-D. Yang, Y.-R. Li, Y.-C. Lee, "Synthesis of r-GO/TiO2 composites via the UV-assisted photocatalytic reduction of graphene oxide,", Appl. Surf. Sci. vol. 380 (2016) 249–256, https://doi.org/10.1016/j.apsusc.2016.01.118.
[64] S. Sakarkar, S. Muthukumaran, V. Jegatheesan, "Evaluation of polyvinyl alcohol (PVA) loading in the PVA/titanium dioxide (TiO2) thin film coating on polyvinylidene fluoride (PVDF) membrane for the removal of textile dyes,", Chemosphere vol. 257 (2020), 127144 https://doi.org/10.1016/j.chemosphere.2020.127144.
[65] X. Li, A. Janke, P. Formanek, A. Fery, M. Stamm, B.P. Tripathi, "High permeation and antifouling polysulfone ultrafiltration membranes with in situ synthesized silica nanoparticles,", Mater. Today Commun. vol. 22 (2020), 100784 https://doi.org/10.1016/j.mtcomm.2019.100784.
[66] J. Wiszniowski, D. Robert, J. Surmacz-Gorska, K. Miksch, J.-V. Weber, "Photocatalytic mineralization of humic acids with TiO 2: Effect of pH, sulfate and chloride anions,", Int. J. Photo vol. 5 (2) (2003) 69–74, https://doi.org/10.1155/S1110662×03000151.
[67] C. Zhu, J. Shi, S. Xu, M. Ishimori, J. Sui, H. Morikawa, "Design and characterization of self-cleaning cotton fabrics exploiting zinc oxide nanoparticle-triggered photocatalytic degradation,", Cellulose vol. 24 (6) (2017) 2657–2667, https://doi.org/10.1007/s10570-017-1289-7.
[68] Z. Xu, T. Wu, J. Shi, K. Teng, W. Wang, M. Ma, J. Li, X. Qian, C. Li, J. Fan, Photocatalytic antifouling PVDF ultrafiltration membranes based on synergy of graphene oxide and TiO2 for water treatment, J. Membr. Sci. vol. 520 (2016) 281–293, https://doi.org/10.1016/j.memsci.2016.07.060.
[69] I. Ratman, T.D. Kusworo, D.P. Utomo, D.A. Azizah, W.A. Ayodyasena, "Petroleum refinery wastewater treatment using three steps modified nanohybrid membrane coupled with ozonation as integrated pre-treatment,", J. Environ. Chem. Eng. vol. 8 (4) (2020), 103978 https://doi.org/10.1016/j.jece.2020.103978.
[70] S.G. Babu, P. Karthik, M.C. John, S.K. Lakhera, M. Ashokkumar, J. Khim, B. Neppolian, Synergistic effect of sono-photocatalytic process for the degradation of organic pollutants using CuO-TiO2/rGO, Ultrason. Sonochem. vol. 50 (2019) 218–223, https://doi.org/10.1016/j.ultsonch.2018.09.021.